Research Square

Preprints are preliminary reports that have not undergone peer review.
They should not be considered conclusive, used to inform clinical practice,
or referenced by the media as validated information.

A load-coupled DMDc method for long-term aerodynamic load prediction in controlled fluid–structure interaction systems

Haowei Du
Xi'an Jiaotong University https://orcid.org/0009-0001-7975-5101
Tianyi Wang
Xi'an Jiaotong University
Zhen Liu
liuz@mail.xjtu.edu.cn

Xi'an Jiaotong University
Chenxu Jin
Xi'an Jiaotong University
Linyang Li
Xi'an Jiaotong University
Yanming Zhang
Xi'an Jiaotong University
Xiurui Ding
Xi'an Jiaotong University

Research Article

Keywords: Fluid–structure interaction, reduced-order modeling, dynamic mode decomposition with control, aerodynamic load prediction

Posted Date: November 2nd, 2026

DOI: https://doi.org/10.21203/rs.3.rs-11563727/v1

License: This work is licensed under a Creative Commons Attribution 4.0 International License.
Read Full License

Additional Declarations: The authors declare no competing interests.

A load-coupled DMDc method for long-term aerodynamic load prediction in controlled fluid–structure interaction systems

Haowei Du[a], Tianyi Wang[a], Zhen Liu[a,*], Chenxu Jin[a], Linyang Li[a], Yanming Zhang[a] and Xiurui Ding[a]

[a]State Key Laboratory for Strength and Vibration of Mechanical Structures Shaanxi Key Laboratory of Environment and Control for Flight Vehicle School of Aerospace Engineering Xi'an Jiaotong University Xi'an Shaanxi 710049 China

ARTICLE INFO

Keywords:
Fluid–structure interaction
Reduced-order modeling
Dynamic mode decomposition with control
Aerodynamic load prediction

ABSTRACT

In controlled fluid–structure interaction (FSI) systems, nonlinear coupling between fluid loads and structural motion complicates reduced-order modeling and limits aerodynamic load prediction accuracy under different control inputs. To address the limited ability of dynamic mode decomposition with control (DMDc) to capture nonlinear dynamics, this study proposes a load-coupled DMDc (LC-DMDc) method that incorporates nonlinear load effects into state evolution. The method combines proper orthogonal decomposition of the flow, structural motion, and interface loads with a radial basis function mapping, so that the predicted load coefficients provide nonlinear corrections to DMDc state evolution. The resulting model preserves displacement–velocity kinematic relations and is jointly optimized using multistep state and aerodynamic load prediction errors to improve long-term prediction accuracy. For a piezoelectrically actuated flat-plate airfoil, models are trained on frequency-sweep data from high-fidelity FSI simulations and evaluated against standard DMDc and three representative methods under frequency-sweep, sinusoidal inputs with piecewise-constant frequencies, multisine, and step excitations. Over continuous predictions spanning 140 s, aerodynamic force and moment errors relative to high-fidelity simulations do not exceed 7.33%, and wingtip displacement errors remain within 1.25% across all four cases. Compared with the best-performing baseline for each case and response component, LC-DMDc achieves error reductions of up to 75.1%. The method improves the accuracy of long-term aerodynamic load predictions and supports rapid response prediction and control-oriented modeling for controlled FSI systems.

1. Introduction

Fluid–structure interaction (FSI) occurs widely in flexible wings, wind turbine blades, and energy harvesters driven by flow-induced vibrations, making it an important problem in aerospace and energy engineering. The interaction between fluid loads and structural deformation affects system performance and structural safety and involves fundamental questions concerning unsteady flow, structural instability, and energy transfer. Accurately describing and effectively controlling FSI responses therefore has both scientific and engineering significance [1, 2].

Active control provides an important means of regulating loads and motion in FSI systems to improve performance. In aerospace engineering, active wing morphing and control-surface deflection can alleviate maneuver- and gust-induced aerodynamic loads and suppress vibrations of flexible structures [3, 4]. In offshore wind energy, blade pitch and generator torque control can coordinate rotor aerodynamic loads and floating-platform motion, reducing load fluctuations and stabilizing power output [5, 6]. In bioinspired underwater robotics, actively driving a flexible body exploits the interaction between structural deformation and the surrounding flow to achieve rapid swimming and agile turning [7]. These applications show that controlled FSI supports not only load alleviation and vibration suppression but also improvements in propulsion and maneuverability. However, these control tasks share a common modeling challenge: control-induced structural motion changes the flow and fluid loads, which in turn affect the structural response. This nonlinear coupling makes control effects difficult to predict. Meanwhile, the high computational cost of high-fidelity FSI simulations limits their repeated use in control optimization. Therefore, reduced-order models that balance nonlinear representation, continuous prediction accuracy, and computational efficiency are needed to predict loads and motion under different control inputs and support repeated input adjustments in model predictive control [4, 6].

*Corresponding author
liuz@mail.xjtu.edu.cn (Z. Liu)

Modeling approaches for controlled FSI systems mainly involve either reducing physics-based models or identifying dynamics from response data. The former couples unsteady aerodynamic and structural dynamics models, then applies linearization and model reduction to construct models for control. For example, He and Su [8] developed a linear parameter-varying model for vibration suppression and attitude control of highly flexible aircraft. Ang and Ng [9] coupled an unsteady vortex-lattice method with a finite element model and applied balanced truncation to support gust alleviation control of a flexible flying wing. Data-driven methods instead identify dynamical relationships from numerical simulations or experimental responses. Hickner et al. [1] used the eigensystem realization algorithm (ERA) to construct a flexible-wing model for lift tracking subject to deformation constraints. Brown et al. [10] combined convolution and Volterra models for nonlinear aeroelastic prediction and control design. Candon et al. [11] interpolated the parameters of sparse higher-order models to predict limit-cycle oscillations under different dynamic pressures and freeplay conditions. In addition, Wu et al. [3] combined recurrent neural networks with a dynamic inversion model for active load alleviation. Li et al. [12] used a reduced-order stall-flutter model as a reinforcement learning training environment and validated the control performance in coupled fluid–structure–control simulations. These studies show that data-driven reduced-order models can effectively support prediction and control of controlled FSI systems, although different modeling approaches have different limitations. Intrusive model reduction is primarily limited by its dependence on the internal operators and solver interfaces of the full-order model: constructing the reduced-order model requires access to the discretized equations and their projection. Such methods are therefore difficult to apply directly when only experimental measurements are available or solver source code is inaccessible [13, 14]. Nonintrusive methods avoid access to full-order operators, but data preparation and identification can still be costly. For example, ERA-based methods require generating or recovering impulse responses and constructing Hankel matrices. Data acquisition, matrix storage, and decomposition costs increase with the number of input and output channels or the response decay time [15, 16]. Thus, intrusive methods are constrained by access to internal model information, whereas some nonintrusive methods are limited by specific training-data requirements and offline computational costs. To address dependence on full-order operators and the preparation of impulse-response data, dynamic mode decomposition with control (DMDc) offers a direct data-driven modeling approach. It requires neither access to internal solver operators nor prior recovery of impulse responses. Instead, it identifies reduced-order dynamics through dimensionality reduction and joint regression of state and control-input time series collected under excitation. This reduces dependence on internal solver information and dedicated impulse-response data, facilitating prediction and control-oriented modeling of controlled FSI systems [17].

DMDc jointly identifies the state-transition and input matrices to separate intrinsic system dynamics from external input effects. It uses low-dimensional modes to construct a state-space model for recursive prediction and control design [18, 19]. Its effectiveness was first demonstrated for low- and high-dimensional controlled linear systems [17], followed by applications to fluid, structural, and aeroelastic systems [20–22]. Its main advantages are the ability to directly process high-dimensional time series, explicitly retain control inputs, and support rapid prediction in a compact state-space form [23]. However, standard DMDc assumes linear evolution in a fixed state representation, limiting its description of nonlinear dynamics [24]. To address these issues, extensions have been developed through state construction, nonlinear representation, and stability constraints [25–27]. For mechanical vibration systems, sd-DMDc augments the state with scaled displacement derivatives and uses forward–backward identification to mitigate noise. It improved modeling accuracy under partial observation in simulations and experiments on a multi-input, multi-output cantilever plate [28]. For nonlinear systems, DMDc combined with Gaussian process regression uses nonlinear residuals to correct the linear model. It outperformed DMDc alone in predictions of a controlled Stuart–Landau system and a turbulent boundary layer [29]. Through optimization-based identification and eigenvalue constraints, cOptDMDc suppresses spurious growing modes in systems that should be stable, improving prediction stability over long trajectories [30]. Furthermore, ResDMDc selects modes using spectral residuals in a space of nonlinear observables. For a controlled nonlinear aeroelastic panel, a Van der Pol oscillator, and the Burgers equation, it achieved better predictions with fewer modes than conventional truncation strategies [31]. For controlled FSI modeling, aDMDc incorporates algebraic relationships and connects local models at different operating conditions through interpolation. This enabled real-time prediction of nonlinear aeroelastic responses and model predictive control of morphing wings, extending the applicability of a single linear model [32].

These studies have improved the nonlinear representation, noise robustness, and rollout stability of standard DMDc, but maintaining quantitative accuracy in aerodynamic load predictions over continuous rollouts remains challenging. For example, a recent study of transonic wing pressure prediction found that DMDc was less accurate than the nonlinear models considered under high-frequency excitation, and rollout errors further affected pitching-moment

predictions [21]. For FSI systems, aerodynamic load prediction also involves interactions between loads and structural motion and therefore requires accurate descriptions of the temporal evolution of coupled responses. A surface-pressure DMDc model overestimated heave damping in a transonic wing case, causing the coupled response to gradually deviate from the reference after approximately 2.5 s [33]. These results indicate that long-term aerodynamic load prediction requires not only improved nonlinear representation but also attention to the accuracy of coupled response evolution and the effects of prediction errors on aerodynamic force and moment outputs during continuous rollouts. To address this issue, some studies use observations acquired during operation to update models and reduce model prediction errors. Online DMD updates dynamical models using new observations and has been applied to control of flow past a circular cylinder and adaptive quadrotor control [34, 35]. DMDc combined with Kalman filtering updates state estimates using observations, improving flow control under noisy conditions [25]. DMDc-based model predictive control uses the current measured state to optimize a finite-horizon control sequence on a receding horizon [36]. Through continual observation feedback, these strategies mitigate the effects of model mismatch on closed-loop operation. However, in the controlled FSI prediction task considered here, the model receives only the initial state and future control inputs. Subsequent aerodynamic loads and structural responses must be predicted recursively without correction using subsequent reference states. This task requires the model to capture nonlinear load variations induced by control inputs while maintaining accurate predictions of response amplitudes and temporal evolution over long rollouts. Therefore, it is necessary to combine nonlinear load representation with multistep dynamical system identification to improve the accuracy of long-term aerodynamic load predictions under different control inputs, without using subsequent ground-truth states to correct the predictions.

To this end, this study proposes load-coupled dynamic mode decomposition with control (LC-DMDc) for long-term aerodynamic load prediction in controlled FSI systems. The method first applies proper orthogonal decomposition to reduce the dimensions of the flow, structural motion, and interface loads. Radial basis functions define a nonlinear mapping from the system state and control input to low-dimensional load coefficients. The predicted coefficients provide a nonlinear correction to DMDc state evolution and are also used to reconstruct interface loads and calculate aerodynamic forces and moments. During structural state evolution, the displacement–velocity relation is explicitly enforced to maintain kinematic consistency. The resulting model is then trained by jointly optimizing the load-mapping and state-transition parameters. The training objective primarily comprises multistep prediction errors in states, aerodynamic forces, and moments, supplemented by an auxiliary loss for power prediction. Finally, prediction performance is evaluated through long-term predictions under different control inputs and comparisons with representative DMDc methods. Ablation studies assess the roles of the nonlinear load mapping, kinematic constraints, and training strategy. The remainder of this paper is organized as follows. Section 2 reviews the theoretical foundations of standard DMDc and presents the LC-DMDc formulation.Section 3 describes the computational models, together with the training and test conditions. Section 4 compares the accuracy of aerodynamic load and structural response predictions under frequency-sweep excitation, sinusoidal inputs with piecewise-constant frequencies, multisine inputs, and step inputs, and examines the role of each component through ablation studies. Section 5 summarizes the main work and conclusions.

2. Load-coupled dynamic mode decomposition with control

2.1. Theoretical foundations of DMDc

Dynamic mode decomposition (DMD) identifies an approximate linear evolution operator from state snapshots at adjacent time instants to extract the system's dynamical features and predict its temporal evolution. However, for systems subject to external control, regression based solely on state snapshots may conflate control-input effects with the identified state evolution operator. Dynamic mode decomposition with control (DMDc) explicitly incorporates input data into the identification process to jointly estimate the state-transition and input matrices [17]. Consider a system sampled at a fixed time interval, with state vector $\boldsymbol{x}_k \in \mathbb{R}^n$ and control input $\boldsymbol{u}_k \in \mathbb{R}^\ell$. Its discrete-time evolution is approximated by

$$\boldsymbol{x}_{k+1} = \boldsymbol{A}\boldsymbol{x}_k + \boldsymbol{B}\boldsymbol{u}_k, \tag{1}$$

where $\boldsymbol{A} \in \mathbb{R}^{n\times n}$ is the state-transition matrix and $\boldsymbol{B} \in \mathbb{R}^{n\times \ell}$ is the input matrix. Both matrices are unknown and are determined jointly from the state and control-input data. The consecutively sampled states and their corresponding

inputs form the snapshot matrices

$$\begin{aligned} \boldsymbol{X} &= \begin{bmatrix} \boldsymbol{x}_0 & \boldsymbol{x}_1 & \cdots & \boldsymbol{x}_{m-1} \end{bmatrix}, \\ \boldsymbol{X}' &= \begin{bmatrix} \boldsymbol{x}_1 & \boldsymbol{x}_2 & \cdots & \boldsymbol{x}_{m} \end{bmatrix}, \\ \boldsymbol{Y} &= \begin{bmatrix} \boldsymbol{u}_0 & \boldsymbol{u}_1 & \cdots & \boldsymbol{u}_{m-1} \end{bmatrix}. \end{aligned} \tag{2}$$

The two state snapshot matrices each contain m columns and are shifted by one sampling interval; each input column corresponds to the associated state transition. Equation (1) then gives

$$\boldsymbol{X}' \approx \boldsymbol{A}\boldsymbol{X} + \boldsymbol{B}\boldsymbol{Y} = \begin{bmatrix} \boldsymbol{A} & \boldsymbol{B} \end{bmatrix} \begin{bmatrix} \boldsymbol{X} \\ \boldsymbol{Y} \end{bmatrix} = \boldsymbol{G}\boldsymbol{\Omega}, \tag{3}$$

where the joint operator and augmented snapshot matrix are defined as

$$\boldsymbol{G} = \begin{bmatrix} \boldsymbol{A} & \boldsymbol{B} \end{bmatrix}, \qquad \boldsymbol{\Omega} = \begin{bmatrix} \boldsymbol{X} \\ \boldsymbol{Y} \end{bmatrix}. \tag{4}$$

Joint identification of the state-transition and input matrices can therefore be formulated as the least-squares problem

$$\min_{\boldsymbol{A},\boldsymbol{B}} \left\| \boldsymbol{X}' - \boldsymbol{G}\boldsymbol{\Omega} \right\|_{\mathrm{F}}^2, \tag{5}$$

where the subscript F denotes the Frobenius norm. The minimum-norm least-squares solution is

$$\boldsymbol{G}_{\mathrm{LS}} = \boldsymbol{X}'\boldsymbol{\Omega}^{\dagger}, \tag{6}$$

where $\boldsymbol{\Omega}^{\dagger}$ denotes the Moore–Penrose pseudoinverse of the augmented data matrix. For high-dimensional data, a truncated singular value decomposition (SVD) provides a low-rank approximation of the augmented snapshot matrix:

$$\boldsymbol{\Omega} \approx \widetilde{\boldsymbol{U}}\,\widetilde{\boldsymbol{\Sigma}}\,\widetilde{\boldsymbol{V}}^{\mathrm{T}}. \tag{7}$$

Retaining the leading p nonzero singular values and their associated singular vectors yields the truncated approximation of the joint operator,

$$\overline{\boldsymbol{G}} = \boldsymbol{X}'\widetilde{\boldsymbol{V}}\,\widetilde{\boldsymbol{\Sigma}}^{-1}\widetilde{\boldsymbol{U}}^{\mathrm{T}}. \tag{8}$$

The left singular vector matrix is partitioned according to the state and input dimensions:

$$\widetilde{\boldsymbol{U}} = \begin{bmatrix} \widetilde{\boldsymbol{U}}_{\mathrm{x}} \\ \widetilde{\boldsymbol{U}}_{\mathrm{u}} \end{bmatrix}, \qquad \widetilde{\boldsymbol{U}}_{\mathrm{x}} \in \mathbb{R}^{n\times p}, \qquad \widetilde{\boldsymbol{U}}_{\mathrm{u}} \in \mathbb{R}^{\ell\times p}. \tag{9}$$

The state-transition and input matrices are then estimated as

$$\begin{aligned} \overline{\boldsymbol{A}} &= \boldsymbol{X}'\widetilde{\boldsymbol{V}}\,\widetilde{\boldsymbol{\Sigma}}^{-1}\widetilde{\boldsymbol{U}}_{\mathrm{x}}^{\mathrm{T}}, \\ \overline{\boldsymbol{B}} &= \boldsymbol{X}'\widetilde{\boldsymbol{V}}\,\widetilde{\boldsymbol{\Sigma}}^{-1}\widetilde{\boldsymbol{U}}_{\mathrm{u}}^{\mathrm{T}}. \end{aligned} \tag{10}$$

These matrices still correspond to the original state dimension. Constructing a reduced-order model therefore requires a low-dimensional projection basis for the state space. The left singular vectors of the augmented matrix contain both state and input information and thus cannot be used directly as a state-space projection basis. A second truncated SVD is therefore applied to the successor-state snapshot matrix:

$$\boldsymbol{X}' \approx \widehat{\boldsymbol{U}}\,\widehat{\boldsymbol{\Sigma}}\,\widehat{\boldsymbol{V}}^{\mathrm{T}}, \qquad \widehat{\boldsymbol{U}} \in \mathbb{R}^{n\times r}. \tag{11}$$

The r retained left singular vectors span a low-dimensional state subspace. The reduced state and approximate reconstruction of the original state are given by

$$\widetilde{\boldsymbol{x}}_k = \widehat{\boldsymbol{U}}^{\mathrm{T}}\boldsymbol{x}_k, \qquad \boldsymbol{x}_k \approx \widehat{\boldsymbol{U}}\widetilde{\boldsymbol{x}}_k. \tag{12}$$

Projecting the state evolution onto this subspace gives the reduced state-transition and input matrices:

$$\begin{aligned}\widetilde{\boldsymbol{A}} &= \widehat{\boldsymbol{U}}^{\mathrm{T}}\overline{\boldsymbol{A}}\widehat{\boldsymbol{U}} = \widehat{\boldsymbol{U}}^{\mathrm{T}}\boldsymbol{X}'\widetilde{\boldsymbol{V}}\widetilde{\boldsymbol{\Sigma}}^{-1}\widetilde{\boldsymbol{U}}_{\mathrm{x}}^{\mathrm{T}}\widehat{\boldsymbol{U}},\\ \widetilde{\boldsymbol{B}} &= \widehat{\boldsymbol{U}}^{\mathrm{T}}\overline{\boldsymbol{B}} = \widehat{\boldsymbol{U}}^{\mathrm{T}}\boldsymbol{X}'\widetilde{\boldsymbol{V}}\widetilde{\boldsymbol{\Sigma}}^{-1}\widetilde{\boldsymbol{U}}_{\mathrm{u}}^{\mathrm{T}}.\end{aligned} \tag{13}$$

The resulting controlled reduced-order state-space model is

$$\widetilde{\boldsymbol{x}}_{k+1} = \widetilde{\boldsymbol{A}}\widetilde{\boldsymbol{x}}_k + \widetilde{\boldsymbol{B}}\boldsymbol{u}_k, \tag{14}$$

where $\widetilde{\boldsymbol{A}} \in \mathbb{R}^{r\times r}$ and $\widetilde{\boldsymbol{B}} \in \mathbb{R}^{r\times \ell}$. Given an initial state and a future control-input sequence, Eq. (14) predicts the reduced state recursively, and Eq. (12) reconstructs the original state. The truncation ranks p and r correspond to the augmented regression space and state reconstruction space, respectively, and can be selected based on the singular value distributions and prediction validation results. Eigendecomposition of the reduced state-transition matrix gives

$$\widetilde{\boldsymbol{A}}\boldsymbol{W} = \boldsymbol{W}\boldsymbol{\Lambda}, \tag{15}$$

where $\boldsymbol{\Lambda}$ contains the discrete-time eigenvalues and the columns of $\boldsymbol{W}$ are the corresponding eigenvectors. For nonzero eigenvalues, the corresponding DMDc modes are recovered as

$$\boldsymbol{\Phi} = \boldsymbol{X}'\widetilde{\boldsymbol{V}}\widetilde{\boldsymbol{\Sigma}}^{-1}\widetilde{\boldsymbol{U}}_{\mathrm{x}}^{\mathrm{T}}\widehat{\boldsymbol{U}}\boldsymbol{W}. \tag{16}$$

The eigenvalues and modes characterize growth, decay, and oscillations associated with the identified state-transition operator, while the input matrix retains the effects of control on state evolution. DMDc thus converts state and input snapshots into a reduced-order dynamical model for modal analysis and recursive prediction.

2.2. Mathematical formulation of LC-DMDc

Load-coupled dynamic mode decomposition with control (LC-DMDc) introduces a nonlinear load mapping based on radial basis functions into the DMDc framework. The predicted low-dimensional load coefficients provide a correction to state evolution and are used to compute aerodynamic forces and moments, enhancing the representation of nonlinear FSI responses within a compact state space. The displacement–velocity relation is also explicitly enforced during structural state evolution to maintain kinematic consistency. Let $\boldsymbol{a}_k$, $\boldsymbol{q}_k$, and $\boldsymbol{v}_k$ denote the reduced coordinates of the flow, structural displacement, and structural velocity, respectively. Projection onto fixed proper orthogonal decomposition (POD) bases gives

$$\boldsymbol{a}_k = \boldsymbol{\Phi}_{\mathrm{f}}^{\mathrm{T}}\frac{\boldsymbol{w}_k}{U_{\mathrm{ref}}}, \qquad \boldsymbol{q}_k = \boldsymbol{\Phi}_{\mathrm{s}}^{\mathrm{T}}\frac{\boldsymbol{d}_k}{L_{\mathrm{ref}}}, \qquad \boldsymbol{v}_k = \boldsymbol{\Phi}_{\mathrm{s}}^{\mathrm{T}}\frac{\dot{\boldsymbol{d}}_k}{U_{\mathrm{ref}}}, \tag{17}$$

where $\boldsymbol{w}_k$ is the flow velocity vector, $\boldsymbol{d}_k$ and $\dot{\boldsymbol{d}}_k$ are the structural nodal displacement and velocity vectors, $\boldsymbol{\Phi}_{\mathrm{f}}$ and $\boldsymbol{\Phi}_{\mathrm{s}}$ are the flow and structural POD bases, and U_{ref} and L_{ref} are the reference velocity and length. Displacement and velocity use the same structural basis to preserve their kinematic relation in the reduced coordinates. Each group of coordinates is standardized using the training-data means and standard deviations to form the model state:

$$\boldsymbol{z}_k = \begin{bmatrix}\boldsymbol{z}_{\mathrm{a},k}\\ \boldsymbol{z}_{\mathrm{q},k}\\ \boldsymbol{z}_{\mathrm{v},k}\end{bmatrix}, \qquad \begin{aligned}\boldsymbol{z}_{\mathrm{a},k} &= \boldsymbol{S}_{\mathrm{a}}^{-1}(\boldsymbol{a}_k - \boldsymbol{\mu}_{\mathrm{a}}),\\ \boldsymbol{z}_{\mathrm{q},k} &= \boldsymbol{S}_{\mathrm{q}}^{-1}(\boldsymbol{q}_k - \boldsymbol{\mu}_{\mathrm{q}}),\\ \boldsymbol{z}_{\mathrm{v},k} &= \boldsymbol{S}_{\mathrm{v}}^{-1}(\boldsymbol{v}_k - \boldsymbol{\mu}_{\mathrm{v}}).\end{aligned} \tag{18}$$

Here, $\boldsymbol{S}_{\mathrm{a}}$, $\boldsymbol{S}_{\mathrm{q}}$, and $\boldsymbol{S}_{\mathrm{v}}$ are diagonal matrices of the corresponding coordinate standard deviations, and $\boldsymbol{\mu}_{\mathrm{a}}$, $\boldsymbol{\mu}_{\mathrm{q}}$, and $\boldsymbol{\mu}_{\mathrm{v}}$ are the corresponding mean vectors. The control input is the normalized voltage, $u_k = V_k/V_{\mathrm{ref}}$. To represent interface loads in a low-dimensional space, the fluid forces acting on the structural nodes are expressed as

$$\widehat{\boldsymbol{f}}_k = \boldsymbol{f}_0 + \boldsymbol{L}_{\mathrm{f}}\boldsymbol{c}_k, \tag{19}$$

where $\boldsymbol{f}_0$ is a fixed load offset, $\boldsymbol{L}_{\mathrm{f}}$ is the load reconstruction matrix incorporating the coefficient scaling, and $\boldsymbol{c}_k \in \mathbb{R}^{r_{\mathrm{c}}}$ is the standardized load coefficient vector. For a two-dimensional system with N_{s} structural nodes, the nodal forces are ordered as

$$\boldsymbol{f}_k = \begin{bmatrix} f_{\mathrm{x},1,k} & \cdots & f_{\mathrm{x},N_\mathrm{s},k} & f_{\mathrm{y},1,k} & \cdots & f_{\mathrm{y},N_\mathrm{s},k} \end{bmatrix}^{\mathrm{T}}. \tag{20}$$

The load coefficients depend on both the current state and the control input. To describe their nonlinear relation to the loads, Gaussian radial basis functions are used to construct nonlinear features [37]. These features are combined with the state, control input, and a constant term to define the load coefficient mapping:

$$\boldsymbol{\phi}(\boldsymbol{z}_k, u_k) = \begin{bmatrix} \boldsymbol{z}_k \\ \boldsymbol{\rho}(\boldsymbol{z}_k, u_k) \\ u_k \\ 1 \end{bmatrix}, \qquad \boldsymbol{c}_k = \boldsymbol{W}\boldsymbol{\phi}(\boldsymbol{z}_k, u_k), \tag{21}$$

where $\boldsymbol{W}$ is the load-mapping matrix to be identified. The jth radial basis function has the Gaussian form

$$\rho_j(\boldsymbol{z}_k, u_k) = \exp\left[-\frac{\|\boldsymbol{h}_k - \boldsymbol{\eta}_j\|_2^2}{2\sigma^2}\right], \qquad \boldsymbol{h}_k = \boldsymbol{S}_\mathrm{h}^{-1}\left(\begin{bmatrix} \boldsymbol{P}\boldsymbol{z}_k \\ u_k \end{bmatrix} - \boldsymbol{\mu}_\mathrm{h}\right). \tag{22}$$

Here, $\boldsymbol{P}$ selects the state components used to construct the radial basis functions, while $\boldsymbol{\eta}_j$ and σ are the center and width, respectively. Once the load coefficients are obtained, the flow and structural velocity states are advanced as

$$\begin{bmatrix} \boldsymbol{z}_{\mathrm{a},k+1} \\ \boldsymbol{z}_{\mathrm{v},k+1} \end{bmatrix} = \boldsymbol{A}\boldsymbol{z}_k + \boldsymbol{B}u_k + \boldsymbol{K}\boldsymbol{c}_k + \boldsymbol{b}, \tag{23}$$

where $\boldsymbol{A}$, $\boldsymbol{B}$, and $\boldsymbol{b}$ describe the contributions of the state, input, and constant offset, respectively, and $\boldsymbol{K}$ is the load-coupling matrix to be identified. Substituting Eq. (21) into Eq. (23) gives

$$\begin{bmatrix} \boldsymbol{z}_{\mathrm{a},k+1} \\ \boldsymbol{z}_{\mathrm{v},k+1} \end{bmatrix} = \boldsymbol{A}\boldsymbol{z}_k + \boldsymbol{B}u_k + \boldsymbol{K}\boldsymbol{W}\boldsymbol{\phi}(\boldsymbol{z}_k, u_k) + \boldsymbol{b}. \tag{24}$$

Thus, the nonlinear correction to state evolution is introduced through the low-dimensional load variables. These variables are constrained by both nodal load reconstruction and aerodynamic load prediction, giving the nonlinear term in state evolution and the mechanical outputs a common data source. Structural displacement is advanced from velocity using trapezoidal integration, rather than identified through a separate unconstrained regression. Under the nondimensional definitions in Eq. (17), the reduced displacement and velocity satisfy

$$\boldsymbol{q}_{k+1} = \boldsymbol{q}_k + \frac{\Delta t\, U_\mathrm{ref}}{2L_\mathrm{ref}}(\boldsymbol{v}_k + \boldsymbol{v}_{k+1}). \tag{25}$$

Substituting the standardization relations gives the form used for state evolution:

$$\boldsymbol{z}_{\mathrm{q},k+1} = \boldsymbol{z}_{\mathrm{q},k} + \boldsymbol{\Gamma}(\boldsymbol{z}_{\mathrm{v},k} + \boldsymbol{z}_{\mathrm{v},k+1}) + \boldsymbol{\beta}, \tag{26}$$

where

$$\boldsymbol{\Gamma} = \frac{\Delta t\, U_\mathrm{ref}}{2L_\mathrm{ref}}\boldsymbol{S}_\mathrm{q}^{-1}\boldsymbol{S}_\mathrm{v}, \qquad \boldsymbol{\beta} = \frac{\Delta t\, U_\mathrm{ref}}{L_\mathrm{ref}}\boldsymbol{S}_\mathrm{q}^{-1}\boldsymbol{\mu}_\mathrm{v}. \tag{27}$$

Equations (23) and (26) together define the complete state evolution model. The structural nodal displacements and velocities are reconstructed from the predicted states as

$$\begin{aligned} \widehat{\boldsymbol{d}}_k &= L_\mathrm{ref}\boldsymbol{\Phi}_\mathrm{s}(\boldsymbol{\mu}_\mathrm{q} + \boldsymbol{S}_\mathrm{q}\boldsymbol{z}_{\mathrm{q},k}), \\ \widehat{\dot{\boldsymbol{d}}}_k &= U_\mathrm{ref}\boldsymbol{\Phi}_\mathrm{s}(\boldsymbol{\mu}_\mathrm{v} + \boldsymbol{S}_\mathrm{v}\boldsymbol{z}_{\mathrm{v},k}). \end{aligned} \tag{28}$$

The aerodynamic forces and root moment are computed from the same nodal forces reconstructed by Eq. (19). The position of node i relative to the reference point is

$$\widehat{\boldsymbol{r}}_{i,k} = \boldsymbol{r}_i^0 + \widehat{\boldsymbol{d}}_{i,k} - \boldsymbol{r}_\mathrm{ref}. \tag{29}$$

The mechanical outputs are then

$$\widehat{\boldsymbol{y}}_k = \begin{bmatrix} \widehat{F}_{\mathrm{x},k} \\ \widehat{F}_{\mathrm{y},k} \\ \widehat{M}_{\mathrm{z},k} \end{bmatrix} = \begin{bmatrix} \displaystyle\sum_{i=1}^{N_\mathrm{s}} \widehat{f}_{\mathrm{x},i,k} \\ \displaystyle\sum_{i=1}^{N_\mathrm{s}} \widehat{f}_{\mathrm{y},i,k} \\ \displaystyle\sum_{i=1}^{N_\mathrm{s}} \left(\widehat{r}_{\mathrm{x},i,k} \widehat{f}_{\mathrm{y},i,k} - \widehat{r}_{\mathrm{y},i,k} \widehat{f}_{\mathrm{x},i,k} \right) \end{bmatrix}. \tag{30}$$

The moment is evaluated using the moment arms in the predicted configuration. The interface power is computed from the nodal forces and structural velocities:

$$\widehat{P}_k = \widehat{\boldsymbol{f}}_k^{\mathrm{T}} \widehat{\boldsymbol{d}}_k. \tag{31}$$

The interface power serves as an auxiliary training constraint on the relation between loads and structural motion. The primary prediction targets remain the aerodynamic loads and their temporal variations. The LC-DMDc parameters to be identified are therefore collected as

$$\boldsymbol{\theta} = \{ \boldsymbol{A}, \boldsymbol{B}, \boldsymbol{K}, \boldsymbol{b}, \boldsymbol{W} \}. \tag{32}$$

The load mapping determines the current load coefficients, the load-coupling term incorporates them into the subsequent state evolution, and nodal load reconstruction converts them into aerodynamic forces and moments. The POD bases, standardization parameters, and radial basis function centers and widths are determined before training and remain fixed during the subsequent joint optimization.

2.3. LC-DMDc model training

Model training comprises data preprocessing, parameter initialization, and multistep joint optimization. The fixed low-dimensional representations are first determined from training snapshots, and ridge regression then provides initial parameter estimates. Finally, the model parameters are jointly updated using state and mechanical output errors from continuous rollouts.

2.3.1. Training data preprocessing

The training data comprise flow velocities, structural nodal displacements and velocities, nodal loads, control inputs, and the corresponding resultant forces and moments. The flow and structural snapshots define the POD representations in Eq. (17), with displacement and velocity sharing the same structural basis. All standardization parameters are computed from the training data. For the interface loads, the training-sample mean is first subtracted, and the centered load snapshot matrix is decomposed by SVD:

$$\boldsymbol{F}_\mathrm{c} = \begin{bmatrix} \boldsymbol{f}_1 - \overline{\boldsymbol{f}} & \cdots & \boldsymbol{f}_N - \overline{\boldsymbol{f}} \end{bmatrix} = \boldsymbol{U}_\mathrm{f} \boldsymbol{\Sigma}_\mathrm{f} \boldsymbol{V}_\mathrm{f}^{\mathrm{T}}. \tag{33}$$

The leading r_c left singular vectors form the load basis $\boldsymbol{\psi}_\mathrm{f}$. The projected nodal load coordinates and their standardized coefficients are

$$\boldsymbol{\alpha}_k = \boldsymbol{\psi}_\mathrm{f}^{\mathrm{T}} (\boldsymbol{f}_k - \overline{\boldsymbol{f}}), \qquad \boldsymbol{c}_k^{\mathrm{data}} = \boldsymbol{S}_\mathrm{c}^{-1} (\boldsymbol{\alpha}_k - \boldsymbol{\mu}_\mathrm{c}). \tag{34}$$

The fixed quantities in Eq. (19) are therefore

$$\boldsymbol{f}_0 = \overline{\boldsymbol{f}} + \boldsymbol{\psi}_\mathrm{f} \boldsymbol{\mu}_\mathrm{c}, \qquad \boldsymbol{L}_\mathrm{f} = \boldsymbol{\psi}_\mathrm{f} \boldsymbol{S}_\mathrm{c}, \tag{35}$$

where $\boldsymbol{S}_\mathrm{c}$ is the diagonal matrix of the load-coordinate standard deviations. The radial basis function centers are selected from the training samples, and the input-feature means and standard deviations are also determined exclusively from the training data. The present implementation retains 20 flow modes, four structural modes, and eight load modes, yielding a 28-dimensional state, and uses 32 radial basis functions. The distance used in the nonlinear features is evaluated using the first four flow-state components, the first two displacement-state components, the first two velocity-state components, and the control input, giving nine components in total. The Gaussian kernel uses $\sigma^2 = 9$. Thus, the feature vector in Eq. (21) has 62 components, and the load-mapping matrix has dimensions 8×62.

2.3.2. State-transition parameter initialization

The feature matrix is constructed from the training states and inputs, with the projected load coefficients as the regression targets:

$$\boldsymbol{\Phi} = \begin{bmatrix} \boldsymbol{\phi}_1 & \cdots & \boldsymbol{\phi}_N \end{bmatrix}, \qquad \boldsymbol{C}_{\text{data}} = \begin{bmatrix} \boldsymbol{c}_1^{\text{data}} & \cdots & \boldsymbol{c}_N^{\text{data}} \end{bmatrix}, \tag{36}$$

where $\boldsymbol{\phi}_k = \boldsymbol{\phi}(\boldsymbol{z}_k, u_k)$. The initial load-mapping matrix is obtained by ridge regression:

$$\boldsymbol{W}_0 = \arg\min_{\boldsymbol{W}} \left[\frac{1}{N} \|\boldsymbol{C}_{\text{data}} - \boldsymbol{W}\boldsymbol{\Phi}\|_{\text{F}}^2 + \lambda_{\text{f}} \|\boldsymbol{W}\boldsymbol{R}_{\phi}\|_{\text{F}}^2 \right], \tag{37}$$

where $\boldsymbol{R}_{\phi}$ is a diagonal penalty matrix whose entry corresponding to the constant feature is zero and whose remaining diagonal entries are one. The initial load predictions at the training samples are then

$$\hat{\boldsymbol{c}}_k^0 = \boldsymbol{W}_0 \boldsymbol{\phi}(\boldsymbol{z}_k, u_k). \tag{38}$$

Adjacent state pairs within the training interval are selected to construct the regression inputs and targets:

$$\boldsymbol{D} = \begin{bmatrix} \boldsymbol{z}_{k_1} & \cdots & \boldsymbol{z}_{k_M} \\ u_{k_1} & \cdots & u_{k_M} \\ \hat{\boldsymbol{c}}_{k_1}^0 & \cdots & \hat{\boldsymbol{c}}_{k_M}^0 \\ 1 & \cdots & 1 \end{bmatrix}, \qquad \boldsymbol{T} = \begin{bmatrix} \boldsymbol{\xi}_{k_1+1} & \cdots & \boldsymbol{\xi}_{k_M+1} \end{bmatrix}, \tag{39}$$

where

$$\boldsymbol{\xi}_k = \begin{bmatrix} \boldsymbol{z}_{\text{a},k} \\ \boldsymbol{z}_{\text{v},k} \end{bmatrix}. \tag{40}$$

The state-transition parameter matrix is defined as

$$\boldsymbol{\Theta} = \begin{bmatrix} \boldsymbol{A} & \boldsymbol{B} & \boldsymbol{K} & \boldsymbol{b} \end{bmatrix}, \tag{41}$$

and its initial estimate is obtained by ridge regression:

$$\boldsymbol{\Theta}_0 = \arg\min_{\boldsymbol{\Theta}} \left[\frac{1}{M} \|\boldsymbol{T} - \boldsymbol{\Theta}\boldsymbol{D}\|_{\text{F}}^2 + \lambda_{\text{d}} \|\boldsymbol{\Theta}\boldsymbol{R}_{\text{d}}\|_{\text{F}}^2 \right], \tag{42}$$

where $\boldsymbol{R}_{\text{d}}$ likewise leaves the constant term unpenalized. The present implementation uses $\lambda_{\text{f}} = \lambda_{\text{d}} = 0.01$. State-transition initialization uses coefficients predicted by the load model, rather than the reference load projection coefficients, so that the input form is consistent with subsequent rollouts. Displacement is updated directly using Eq. (26) and is excluded from this regression. Figure 1 summarizes the preprocessing and initialization procedures.

2.3.3. Multistep rollout and parameter updates

After parameter initialization, sliding windows are extracted from the training sequence for multistep prediction. A window starting at sampling index s with a prediction horizon of H steps spans indices s through $s + H$. It contains one initial state and H subsequent prediction targets, corresponding to $H + 1$ consecutive samples. For each window, the model state is initialized only at the start using the corresponding reference state:

$$\hat{\boldsymbol{z}}_{s,0} = \boldsymbol{z}_s^{\text{data}}. \tag{43}$$

Here, the superscript data denotes a reference value from the training data, and $\hat{\boldsymbol{z}}_{s,j}$ is the state predicted after j consecutive steps from index s, corresponding to index $s + j$ in the original sequence. After initialization, the model computes the load coefficients from the current predicted state and the prescribed control input, then obtains the next state using the state-transition equation and the displacement–velocity relation. This process continues for H steps using the predicted states, without reference-state corrections within the window. At each prediction step, the predicted

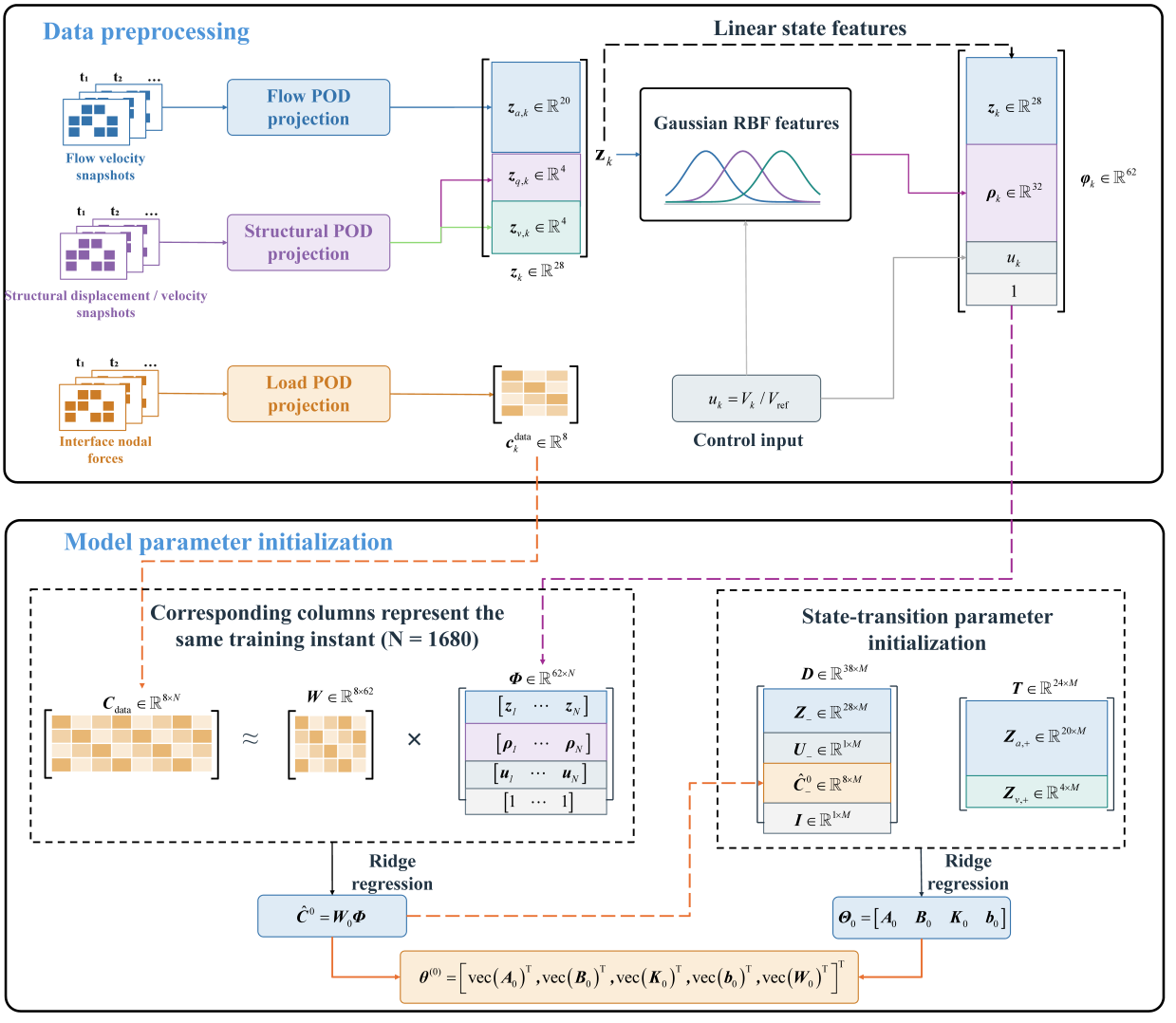


Figure 1: Data preprocessing and model parameter initialization.

state, mechanical outputs, and interface power are compared with their corresponding reference values to define the errors:

$$
\begin{aligned}
\boldsymbol{e}_{\mathrm{z},s,j} &= \hat{\boldsymbol{z}}_{s,j} - \boldsymbol{z}^{\mathrm{data}}_{s+j}, \\
e_{\mathrm{y},i,s,j} &= \frac{\hat{y}_{i,s,j} - y^{\mathrm{data}}_{i,s+j}}{s_{\mathrm{y},i}}, \\
e_{\mathrm{P},s,j} &= \frac{\hat{P}_{s,j} - P^{\mathrm{data}}_{s+j}}{s_{\mathrm{P}}}.
\end{aligned}
\tag{44}
$$

Here, $\boldsymbol{e}_{\mathrm{z},s,j}$ is the reduced-state error vector, while $e_{\mathrm{y},i,s,j}$ and $e_{\mathrm{P},s,j}$ are the normalized mechanical output and interface power errors. The three mechanical outputs are the streamwise aerodynamic force, transverse aerodynamic force, and aerodynamic moment, with $y_1 = F_{\mathrm{x}}$, $y_2 = F_{\mathrm{y}}$, and $y_3 = M_{\mathrm{z}}$. Both $\hat{y}_{i,s,j}$ and $\hat{P}_{s,j}$ are computed from the predicted states and load coefficients within the window. The normalization factors $s_{\mathrm{y},i}$ and s_{P} are the training-set standard deviation of the ith mechanical output and the training-set root mean square of the interface power, respectively; both remain

fixed during optimization. The errors are combined into the loss at a single prediction step:

$$\ell_{s,j} = \frac{\sum_{i=1}^{3} \omega_i e_{\mathrm{y},i,s,j}^2}{\sum_{i=1}^{3} \omega_i} + \frac{\lambda_{\mathrm{z}}}{n_{\mathrm{z}}} \|\boldsymbol{e}_{\mathrm{z},s,j}\|_2^2 + \lambda_{\mathrm{P}} e_{\mathrm{P},s,j}^2, \tag{45}$$

where ω_i are the mechanical output weights, set to $\omega_1 : \omega_2 : \omega_3 = 1 : 1 : 2$, and $n_{\mathrm{z}} = 28$ is the dimension of the complete reduced state. The state and power error weights are $\lambda_{\mathrm{z}} = \lambda_{\mathrm{P}} = 0.1$, and $\|\cdot\|_2$ denotes the Euclidean norm. The first term constrains aerodynamic force and moment predictions, the second constrains reduced-state evolution, and the third provides an auxiliary constraint on the relation between loads and structural motion through the power error. Averaging over all valid prediction windows and the H prediction steps within each window gives the H-step prediction loss:

$$\mathcal{L}_H = \frac{1}{N_H H} \sum_{s \in S_H} \sum_{j=1}^{H} \ell_{s,j}, \tag{46}$$

where S_H is the set of window start indices that allow H prediction steps within the training interval, and N_H is the number of such windows. Successive window starts are separated by 32 sampling steps. To account for both response fitting over a shorter horizon and prediction deviations over a longer horizon, the losses for two prediction lengths are combined as

$$\mathcal{L}_{\mathrm{ms}} = \alpha_{\mathrm{s}} \mathcal{L}_{H_{\mathrm{s}}} + \alpha_{\mathrm{l}} \mathcal{L}_{H_{\mathrm{l}}}, \qquad \alpha_{\mathrm{s}} + \alpha_{\mathrm{l}} = 1, \tag{47}$$

where $H_{\mathrm{s}} = 64$ and $H_{\mathrm{l}} = 256$ are the shorter and longer prediction horizons, with weights $\alpha_{\mathrm{s}} = 0.75$ and $\alpha_{\mathrm{l}} = 0.25$. The two sets of windows are averaged separately using Eq. (46) before their losses are combined.

Multistep joint optimization also includes a mechanical output mapping loss evaluated at the reference states. At training index k, the reference reduced state and control input are supplied to the load mapping:

$$\hat{\boldsymbol{c}}_k^{\mathrm{map}} = \boldsymbol{W} \boldsymbol{\phi}(\boldsymbol{z}_k^{\mathrm{data}}, u_k). \tag{48}$$

The nodal loads are then reconstructed and used with the reference structural configuration to compute the aerodynamic forces and moment:

$$\hat{\boldsymbol{y}}_k^{\mathrm{map}} = \begin{bmatrix} \hat{F}_{\mathrm{x},k}^{\mathrm{map}} \\ \hat{F}_{\mathrm{y},k}^{\mathrm{map}} \\ \hat{M}_{\mathrm{z},k}^{\mathrm{map}} \end{bmatrix}. \tag{49}$$

The corresponding mapping loss is

$$\mathcal{L}_{\mathrm{map}} = \frac{1}{N} \sum_{k \in \mathcal{L}_{\mathrm{train}}} \frac{\sum_{i=1}^{3} \omega_i \left(\dfrac{\hat{y}_{i,k}^{\mathrm{map}} - y_{i,k}^{\mathrm{data}}}{s_{\mathrm{y},i}} \right)^2}{\sum_{i=1}^{3} \omega_i}, \tag{50}$$

where $\mathcal{L}_{\mathrm{train}}$ is the set of training-sample indices, N is its number of samples, and the superscript map denotes a mapping prediction obtained using a reference state as input. The final training objective is

$$\mathcal{L} = \mathcal{L}_{\mathrm{ms}} + \lambda_{\mathrm{map}} \mathcal{L}_{\mathrm{map}}, \tag{51}$$

where the mapping loss weight is $\lambda_{\mathrm{map}} = 0.01$. All loss weights remain fixed throughout optimization. Minimizing the total loss jointly identifies the state-transition and load-mapping parameters. Stacking all parameters to be identified

into a single vector gives the optimization problem:

$$\begin{aligned}\boldsymbol{\theta} &= \left[\mathrm{vec}(\boldsymbol{A})^{\mathrm{T}}, \mathrm{vec}(\boldsymbol{B})^{\mathrm{T}}, \mathrm{vec}(\boldsymbol{K})^{\mathrm{T}}, \mathrm{vec}(\boldsymbol{b})^{\mathrm{T}}, \mathrm{vec}(\boldsymbol{W})^{\mathrm{T}}\right]^{\mathrm{T}},\\ \boldsymbol{\theta}^{*} &= \arg\min_{\boldsymbol{\theta}} \mathcal{L}(\boldsymbol{\theta}),\end{aligned} \tag{52}$$

where $\mathrm{vec}(\cdot)$ stacks the columns of a matrix into a vector, and $\boldsymbol{\theta}^{*}$ denotes the target solution of the optimization problem. At optimization iteration r, all training windows use the current parameters to perform continuous rollouts from their respective reference initial states. The total loss is evaluated from the predictions, and backpropagation through the state evolution gives the parameter gradient:

$$\begin{aligned}\boldsymbol{g}^{(r)} &= \nabla_{\boldsymbol{\theta}}\mathcal{L}\big|_{\boldsymbol{\theta}=\boldsymbol{\theta}^{(r)}}\\ &= \left(\alpha_{\mathrm{s}}\nabla_{\boldsymbol{\theta}}\mathcal{L}_{H_{\mathrm{s}}} + \alpha_{\mathrm{l}}\nabla_{\boldsymbol{\theta}}\mathcal{L}_{H_{\mathrm{l}}} + \lambda_{\mathrm{map}}\nabla_{\boldsymbol{\theta}}\mathcal{L}_{\mathrm{map}}\right)\Big|_{\boldsymbol{\theta}=\boldsymbol{\theta}^{(r)}}.\end{aligned} \tag{53}$$

Here, r is the optimization iteration index, $\boldsymbol{\theta}^{(r)}$ is the current parameter vector, and $\boldsymbol{g}^{(r)}$ is the gradient of the total loss with respect to this vector. The limited-memory BFGS (L-BFGS) method computes the search direction, and a line search determines the step size [38]:

$$\begin{aligned}\boldsymbol{d}^{(r)} &= -\boldsymbol{Q}^{(r)}\boldsymbol{g}^{(r)},\\ \boldsymbol{\theta}^{(r+1)} &= \boldsymbol{\theta}^{(r)} + \eta_r\boldsymbol{d}^{(r)}.\end{aligned} \tag{54}$$

Here, $\boldsymbol{d}^{(r)}$ is the parameter search direction, and $\boldsymbol{Q}^{(r)}$ denotes an inverse Hessian approximation constructed from recent parameter and gradient changes. The step size η_r is determined by backtracking line search to satisfy the Armijo sufficient decrease condition. Following the ordering of the parameter vector, the components of the search direction corresponding to $\boldsymbol{A}$, $\boldsymbol{B}$, $\boldsymbol{K}$, $\boldsymbol{b}$, and $\boldsymbol{W}$ are reshaped into matrices or vectors of the same dimensions, denoted by $\boldsymbol{D}_A^{(r)}$, $\boldsymbol{D}_B^{(r)}$, $\boldsymbol{D}_K^{(r)}$, $\boldsymbol{d}_b^{(r)}$, and $\boldsymbol{D}_W^{(r)}$, respectively. The parameter updates are therefore

$$\begin{aligned}\boldsymbol{A}^{(r+1)} &= \boldsymbol{A}^{(r)} + \eta_r\boldsymbol{D}_A^{(r)},\\ \boldsymbol{B}^{(r+1)} &= \boldsymbol{B}^{(r)} + \eta_r\boldsymbol{D}_B^{(r)},\\ \boldsymbol{K}^{(r+1)} &= \boldsymbol{K}^{(r)} + \eta_r\boldsymbol{D}_K^{(r)},\\ \boldsymbol{b}^{(r+1)} &= \boldsymbol{b}^{(r)} + \eta_r\boldsymbol{d}_b^{(r)},\\ \boldsymbol{W}^{(r+1)} &= \boldsymbol{W}^{(r)} + \eta_r\boldsymbol{D}_W^{(r)}.\end{aligned} \tag{55}$$

After each parameter update, rollouts restart from the initial state of each training window, and the loss and gradient are recomputed. This process continues until the gradient meets the prescribed tolerance or the maximum number of iterations is reached. All parameters are updated jointly with fixed loss weights throughout training, yielding the LC-DMDc model for continuous prediction. Figure 2 summarizes the multistep rollout and parameter update procedures.

3. Computational model

3.1. Fluid domain and parameter settings

A two-dimensional flat-plate airfoil with a chord length of $c = 1$ m is considered. A Cartesian coordinate system is defined with its origin at the initial leading edge, the x-axis aligned with the incoming flow, and the y-axis perpendicular to it. The airfoil initially lies along $0 \le x/c \le 1$, $y/c = 0$, with an angle of attack of 0°. The computational domain spans $-4 \le x/c \le 8$ and $-3 \le y/c \le 3$, giving a streamwise length of $12c$ and a transverse width of $6c$. The inlet is $4c$ upstream of the initial leading edge, the outlet is $7c$ downstream of the initial trailing edge, and the upper and lower boundaries are each $3c$ from the initial chord line, as shown in Figure 3. The fluid is treated as incompressible and Newtonian, with a density of $\rho = 1\,\mathrm{kg\,m^{-3}}$ and a kinematic viscosity of $\nu = 2.5\times10^{-4}\,\mathrm{m^2\,s^{-1}}$. The uniform free-stream velocity is $U_\infty = 0.1\,\mathrm{m\,s^{-1}}$, corresponding to a Reynolds number of $Re = 400$. Two-dimensional direct numerical simulations are performed using a solver developed in OpenFOAM 7 [39], with the fluid–structure interface treated using an immersed boundary method [40]. A Cartesian mesh is locally refined near the airfoil within $-0.2 \le x/c \le 1.8$ and $-1 \le y/c \le 1$.

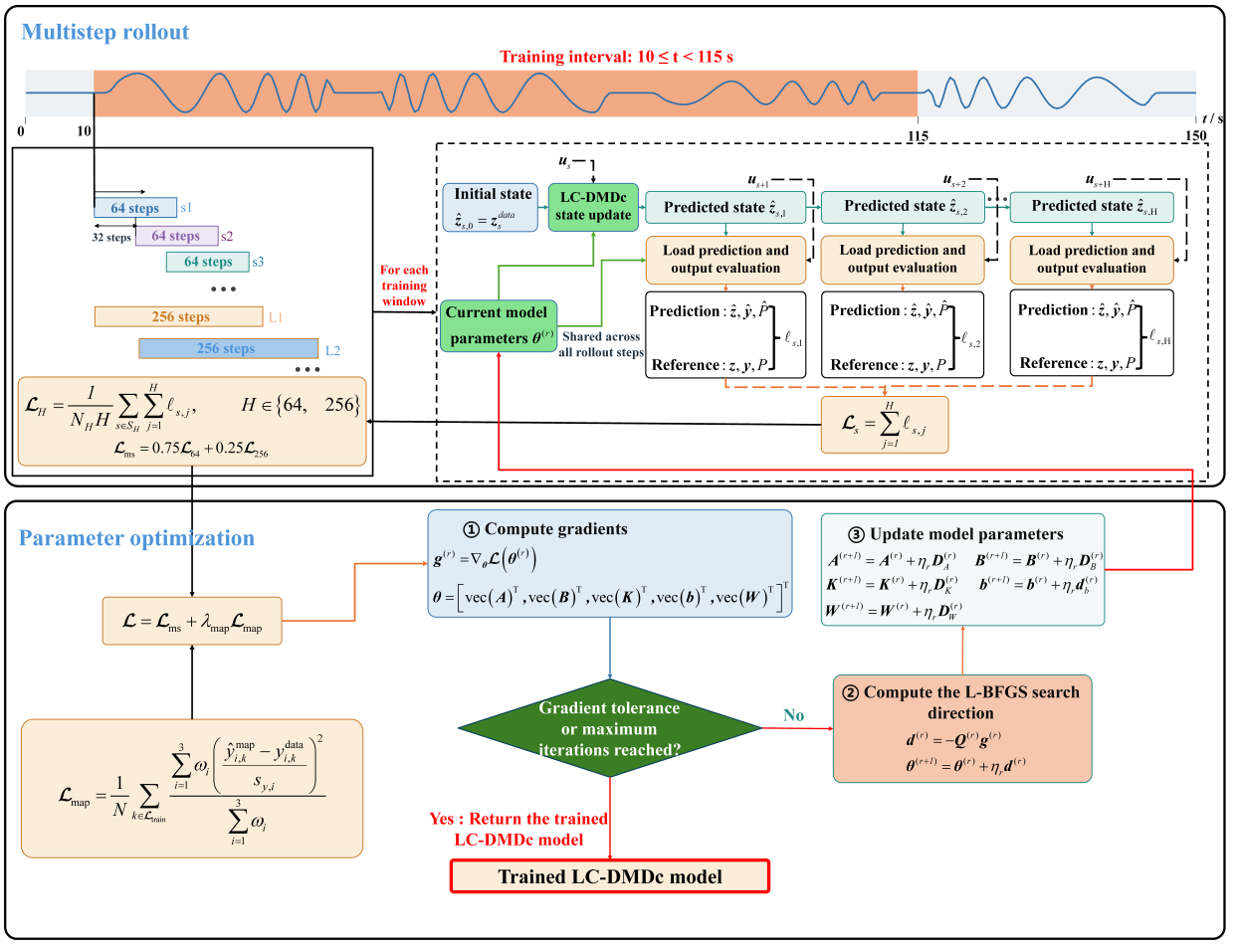


Figure 2: Multistep rollout and parameter updates.

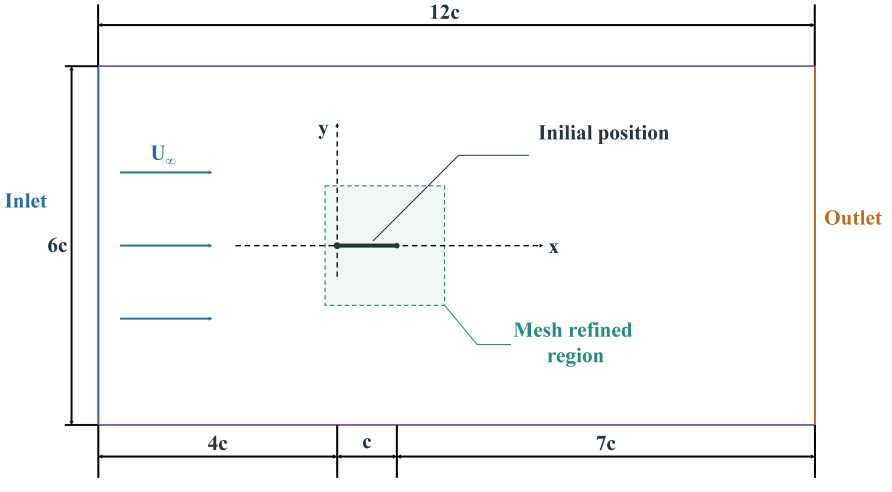


Figure 3: Fluid computational domain.

3.2. Flexible structure model

The flat-plate airfoil is modeled as a two-dimensional cantilever beam of length $c = 1$ m, with its initial centerline along the x-axis. The leading edge is clamped and the trailing edge is free; the axial displacement, transverse displacement, and rotation at the root are all zero. The beam is discretized into 65 elements along the chord, with 66 structural nodes. Its cross-sectional properties are represented by an effective mass, axial rigidity EA, and flexural rigidity EI. The mass ratio is 3, and the rigidities satisfy $EA\,c^2/EI = 10^5$. The piezoelectrically actuated flexible flat-plate airfoil serves as the controlled FSI system in this study. The actuation voltage is the control input, and the piezoelectric bending moment changes the airfoil deformation and hence the fluid loads. This configuration is used to evaluate the ability of LC-DMDc to predict coupled responses and aerodynamic load evolution under control inputs. Piezoelectric actuation is represented by an equivalent model with two layers arranged symmetrically on the upper and lower surfaces. Both layers span $0.10 \le x/c \le 0.35$, covering a length of 0.25 m and lying 0.10 m from the clamped end and 0.65 m from the free end. Their effects are represented through equivalent cross-sectional properties and an actuation bending moment. Figure 4 shows the structural configuration.

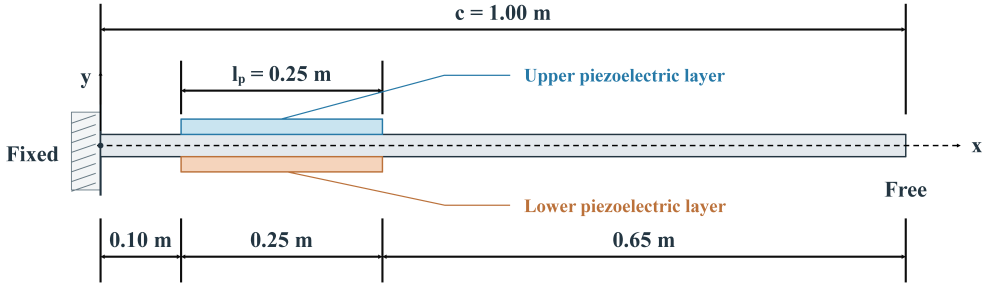


Figure 4: Schematic of the flexible structure.

Structural dynamics are described using a co-rotational Euler–Bernoulli beam model [41], and piezoelectric actuation is introduced into the two-dimensional beam model as an equivalent bending moment. Under the assumptions of thin piezoelectric layers, perfect bonding, and linear piezoelectric constitutive behavior, differential extension and contraction of the upper and lower layers produce bending. The equivalent bending moment is proportional to the actuation voltage [42]:

$$M_{\mathrm{p}}(t) = \Theta_{\mathrm{p}} V(t), \tag{56}$$

where $V(t)$ is the actuation voltage and Θ_{p} is an effective electromechanical coupling coefficient incorporating the piezoelectric material properties and cross-sectional dimensions. The moment is applied over the region covered by the piezoelectric layers and converted into equivalent beam nodal loads to represent actuation in the two-dimensional structural model. The fluid and structural solvers are coupled using an implicit partitioned scheme implemented with preCICE [43]. Within each coupling time window, the structural solver transfers interface displacements to the fluid solver, which returns the updated interface loads. The coupled response is obtained by iterating this exchange. The coupling iterations are accelerated using the interface quasi-Newton inverse least-squares (IQN-ILS) method, with the interface load residual serving as the convergence criterion.

3.3. Validation of the fluid–structure interaction solver

To assess the ability of the FSI solver to capture large deformations and flow-induced vibrations of flexible structures, a two-dimensional inverted flexible flag is used as a benchmark and compared with published results [44, 45]. The flag is clamped at its downstream end and free at its upstream end, and undergoes spontaneous flapping in a uniform flow. No piezoelectric actuation is applied in this case. The Reynolds number is $Re = 200$, the mass ratio is $M_\rho = 0.5$, and the nondimensional bending stiffness is $K_{\mathrm{b}} = 0.35$. The computational domain and boundary conditions are shown in Figure 5. The flag length is $c = 1$ m and the free-stream velocity is $U_\infty = 1\,\mathrm{m\,s^{-1}}$. The domain spans $x/c \in [-16, 16]$ and $y/c \in [-17.5, 17.5]$, with a near-body fluid mesh spacing of $\Delta x = \Delta y = 0.01c$.

Figure 6 shows the time history of the normalized transverse displacement of the free tip's displacement, y_{tip}/c. Following an initial transient, the structure exhibits large-amplitude flapping that alternates between the positive and

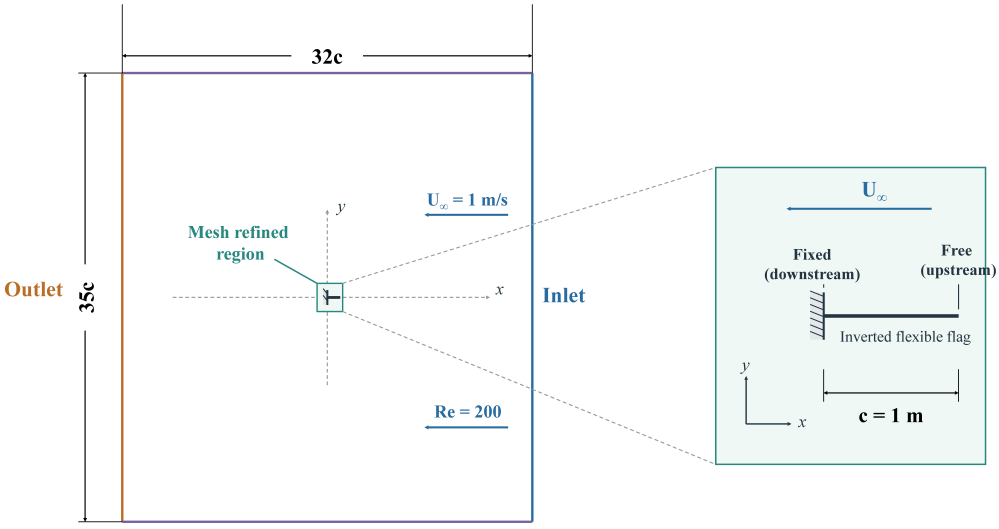


Figure 5: Computational domain, boundary conditions, and structural constraints for the inverted flexible flag.

negative transverse directions. For quantitative comparison, the maximum and minimum tip displacements, $y_{\max}$ and $y_{\min}$, are extracted for each cycle to define the nondimensional single-sided amplitude:

$$a^* = \frac{y_{\max} - y_{\min}}{2c}. \tag{57}$$

The reported amplitude is averaged over the complete cycles. The flapping frequency f is determined from the mean period of the complete cycles, giving the nondimensional frequency

$$St = \frac{fc}{U_\infty}. \tag{58}$$

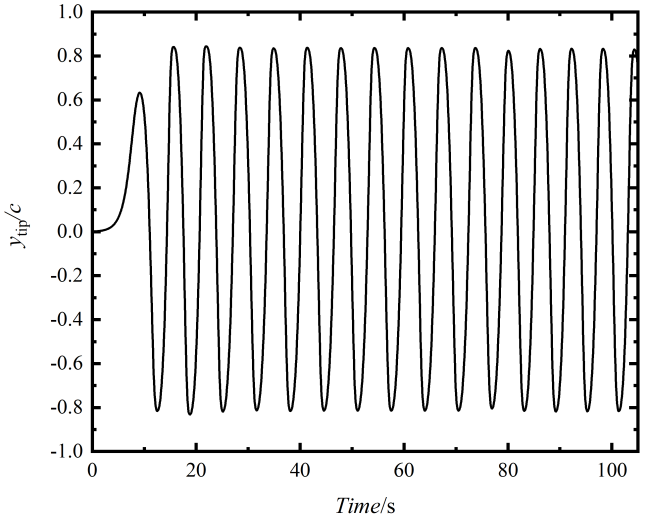


Figure 6: Time history of the transverse tip displacement.

The present simulation yields a nondimensional single-sided amplitude of $a^* = 0.82$ and a nondimensional flapping frequency of $St = 0.171$. To quantify the accuracy, the relative deviations in amplitude and frequency are defined as

$$\begin{aligned} \varepsilon_a &= \frac{|a^* - a_{\mathrm{ref}}|}{|a_{\mathrm{ref}}|} \times 100\%, \\ \varepsilon_{St} &= \frac{|St - St_{\mathrm{ref}}|}{|St_{\mathrm{ref}}|} \times 100\%, \end{aligned} \tag{59}$$

where a_{ref} and St_{ref} are the nondimensional single-sided amplitude and flapping frequency reported in the corresponding reference. These metrics quantify deviations in the deformation amplitude and the time scale of the coupled motion. Table 1 lists the reference values and the relative deviations of the present results.

Table 1
Reference results for the inverted flexible flag and relative deviations of the present simulation.

Reference	a_{ref}	St_{ref}	ε_a (%)	ε_{St} (%)
Goza et al. [44], baseline grid	0.81	0.180	1.23	5.00
Lauber et al. [45]	0.80	0.179	2.50	4.47

Relative to Goza et al. [44], the amplitude and frequency deviations are 1.23% and 5.00%, respectively; relative to Lauber et al. [45], they are 2.50% and 4.47%. The present amplitude is slightly higher than the reference values, while the frequency is slightly lower. For both comparisons, the amplitude deviation is below 3% and the frequency deviation does not exceed 5%. Together with the tip-displacement history in Figure 6, these comparisons assess the solver's performance for the FSI benchmark in terms of large-amplitude oscillatory motion, deformation amplitude, and flapping frequency, providing validation for the subsequent generation of training and test data.

3.4. Training conditions

The piezoelectric actuation voltage is used as the control input, and training and test data are obtained from high-fidelity FSI simulations. The frequency-sweep case lasts 150 s and comprises four logarithmic sweeps with smooth envelopes, as shown in Figure 7. For the jth sweep, the local time is defined as $\tau = t - t_j$, and the voltage is

$$\begin{aligned} V_j(t) &= A_j w(\tau) \sin\left[\phi_j + \frac{2\pi f_{j,0}}{\kappa_j}\left(\mathrm{e}^{\kappa_j \tau} - 1\right)\right], \\ \kappa_j &= \frac{1}{T}\ln\left(\frac{f_{j,1}}{f_{j,0}}\right), \end{aligned} \tag{60}$$

where A_j, t_j, and ϕ_j are the amplitude, start time, and initial phase of the sweep, respectively; $T = 30$ s is the duration of each sweep; and $f_{j,0}$ and $f_{j,1}$ are its initial and final frequencies. The corresponding instantaneous frequency is

$$f_j(\tau) = f_{j,0}\mathrm{e}^{\kappa_j \tau}. \tag{61}$$

Unlike a linear sweep, whose frequency changes at a constant rate, a logarithmic sweep changes frequency at a constant relative rate, varying more slowly at low frequencies and more rapidly at high frequencies. For a given duration and frequency range, a logarithmic sweep therefore allocates more excitation time to the low-frequency range. For example, when sweeping upward from 0.05 to 0.35 Hz over 30 s, a linear sweep traverses the 0.05–0.15 Hz range in 10 s, whereas a logarithmic sweep takes approximately 16.9 s. Because low-frequency responses have longer oscillation periods, logarithmic sweeps are used to increase the excitation time at low frequencies while covering the target frequency band, providing coupled-response data at different frequencies for model identification. A half-cosine envelope lasting 2 s is applied at each end of every sweep to ramp the voltage smoothly up and down, reducing additional transients caused by abrupt input changes. The envelope is defined as

$$w(\tau) = \begin{cases} \dfrac{1 - \cos(\pi\tau/T_{\mathrm{r}})}{2}, & 0 \le \tau < T_{\mathrm{r}}, \\ 1, & T_{\mathrm{r}} \le \tau \le T - T_{\mathrm{r}}, \\ \dfrac{1 - \cos\left[\pi(T-\tau)/T_{\mathrm{r}}\right]}{2}, & T - T_{\mathrm{r}} < \tau \le T, \end{cases} \tag{62}$$

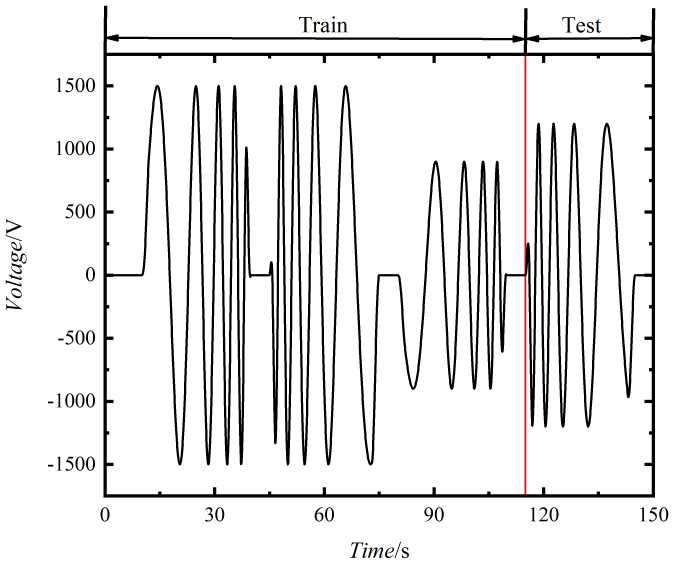


Figure 7: Frequency-sweep voltage input.

where $T_r = 2$ s. The voltage is zero outside the sweep intervals. Table 2 lists the parameters of the four sweeps.

Table 2
Parameters of the frequency-sweep voltage input.

Sweep	Time interval (s)	Amplitude (V)	Initial frequency (Hz)	Final frequency (Hz)	Initial phase
1	10–40	1500	0.05	0.35	0
2	45–75	1500	0.35	0.05	$\pi/2$
3	80–110	900	0.05	0.35	π
4	115–145	1200	0.35	0.05	$\pi/4$

The combination of upward and downward sweeps with different excitation amplitudes drives the system through the target frequency band with different response histories and increases the variation in response amplitude within the training data. Adjacent sweeps are separated by 5 s intervals of zero voltage to capture the free response after unloading. The initial 0–10 s interval is a startup stage with no control input and is excluded from model identification. Data from $10 \leq t < 115$ s are used for training, and the 115–150 s interval is used for the frequency-sweep test. The training interval contains the first three sweeps and their subsequent free responses, whereas the test interval contains the fourth sweep and its subsequent free response. The sampling interval is 0.0625 s, and the last training sample is taken at 114.9375 s. The frequency-sweep test starts from the initial state at 115 s and advances continuously to 150 s under the prescribed voltage input to evaluate the model's ability to predict the subsequent aerodynamic load histories. In addition to the frequency-sweep test, three further input types are considered: piecewise constant-frequency sinusoidal signals, multisine signals, and smooth step pulses. For each of these additional cases, the total simulation duration is 150 s, and prediction accuracy is evaluated over 10–150 s.

DMDc, DMDc+GPR, Hankel-DMDc, and cOptDMDc are selected as comparison methods to assess the improvements offered by LC-DMDc over existing modeling approaches. DMDc serves as the baseline linear model to quantify improvements over the original framework. DMDc+GPR uses Gaussian process regression to correct the state-prediction residuals of a linear model, allowing different approaches to nonlinear modeling to be compared [29]. Hankel-DMDc constructs an augmented state using time-delayed states and inputs, enabling a comparison of how historical information and load coupling affect prediction accuracy [46]. cOptDMDc combines optimization-based identification with eigenvalue constraints to suppress spurious growing modes, allowing its long-term aerodynamic load predictions under stability constraints to be compared with those of LC-DMDc [30]. These methods cover four

modeling strategies: linear identification, nonlinear residual correction, state augmentation with time delays, and stability constraints. All models are identified using data from the same training interval and share the same underlying POD state representation, initial test states, and voltage inputs.

4. Results and discussion

This section evaluates the accuracy of LC-DMDc by comparing its predictions of aerodynamic loads and structural responses with those of several other methods under different voltage inputs. Ablation studies then identify the contribution of each model component to prediction performance and explain why LC-DMDc can accurately predict both aerodynamic loads and structural responses.

4.1. Response predictions under different input excitations

4.1.1. Response predictions under frequency-sweep excitation

This section compares the aerodynamic load and structural displacement predictions of different models for the flat-plate airfoil under the frequency-sweep voltage input introduced in Section 3.4. Figure 8 compares the streamwise aerodynamic force F_x, transverse aerodynamic force F_y, aerodynamic moment M_z, and transverse wingtip displacement predicted by DMDc, DMDc+GPR, Hankel-DMDc, cOptDMDc, and LC-DMDc, with the high-fidelity FSI simulation as the reference.

Figure 9 shows the velocity fields at 137, 140, 143, and 145 s during the frequency-sweep test, with the corresponding plate configurations superimposed. The snapshots at 140 and 145 s are close to the positive and negative displacement extrema, respectively, whereas those at 137 and 143 s correspond to upward and downward plate motion. A low-velocity region extends along the plate and downstream of the trailing edge to form a low-velocity wake. As the plate oscillates, the near-body low-velocity region changes with the structural configuration, the low-velocity band behind the trailing edge shifts laterally and bends, and the velocity distributions on the two sides of the plate adjust accordingly. The overall flow patterns are similar at the four instants, with differences concentrated near the plate and in the near wake, where the location and shape of the low-velocity region and the surrounding velocity distribution change. These snapshots illustrate the local flow adjustments accompanying structural motion and, together with the aerodynamic load and displacement histories, describe the coupled response under frequency-sweep excitation.

The overall responses in Figure 8 show that the oscillation periods of the aerodynamic loads and displacement increase as the sweep frequency decreases, while the wingtip displacement amplitude also changes substantially. All models capture the main oscillatory behavior to some extent, but differ in their predictions of response amplitudes, peak timing, and local load variations. Standard DMDc follows the main variations in transverse aerodynamic force and displacement early in the test but substantially underestimates their amplitudes in the latter half. LC-DMDc agrees well with the reference throughout the test interval, particularly in reproducing the large-amplitude structural motion and associated load variations in the latter half.

The differences are most pronounced in the streamwise aerodynamic force F_x, which exhibits small fluctuations about a mean of approximately 1.074 mN. Although standard DMDc predicts a mean level close to the reference, it does not accurately reproduce the fluctuation amplitudes or timing. Hankel-DMDc introduces additional amplitude deviations in some intervals, while cOptDMDc produces excessively large oscillations. DMDc+GPR improves the prediction of the main fluctuations, and LC-DMDc follows the reference more closely, yielding a root-mean-square error (RMSE) of 0.0161 mN for the streamwise force. This represents reductions of 72.5% and 46.2% relative to DMDc and DMDc+GPR, respectively. The improvement therefore extends beyond the mean load to small-amplitude aerodynamic force fluctuations.

For the transverse aerodynamic force F_y and aerodynamic moment M_z, all models capture the main oscillations early in the test, but amplitude and local waveform deviations develop in the latter half. For example, near 140.6 s, the reference transverse force reaches a positive peak of approximately 5.244 mN, whereas DMDc predicts only about 3.075 mN. LC-DMDc predicts approximately 4.666 mN, substantially reducing the amplitude underestimation. The moment predictions show a similar trend: LC-DMDc tracks the main peaks, troughs, and their evolution more accurately, with an RMSE of 0.282 mN m over the full test interval, 54.6% lower than that of the best-performing comparison method, Hankel-DMDc. However, near the local moment spike at approximately 141 s, the LC-DMDc prediction remains smoother and underestimates the peak, indicating that accurate prediction of the main oscillatory behavior does not fully capture rapid local variations.

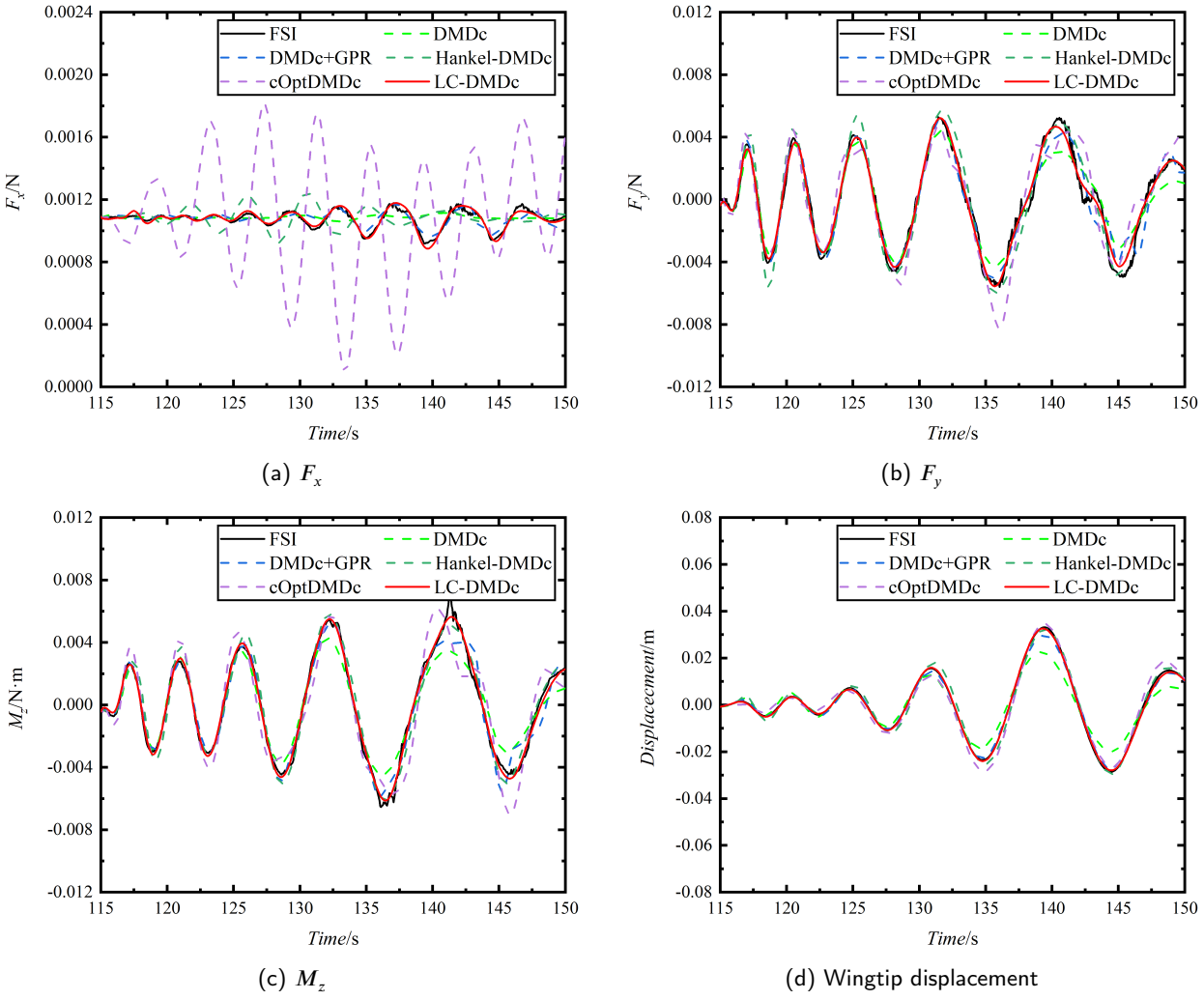


Figure 8: Aerodynamic and structural responses under frequency-sweep excitation: (a) F_x; (b) F_y; (c) M_z; (d) transverse wingtip displacement. FSI denotes the high-fidelity reference solution.

The displacement predictions further demonstrate the advantage of LC-DMDc. At approximately 139.4 s, the reference transverse wingtip displacement reaches about 33.15 mm, whereas DMDc predicts only about 22.51 mm. The LC-DMDc peak is approximately 32.58 mm, closely reproducing the structural deformation amplitude at this stage. DMDc+GPR and Hankel-DMDc both improve on standard DMDc, but LC-DMDc has the lowest displacement error over the full trajectory. Its RMSE is 0.561 mm, 87.4% lower than that of DMDc and 55.1% lower than that of DMDc+GPR. Thus, LC-DMDc improves aerodynamic load prediction while maintaining an accurate description of structural motion.

For a quantitative comparison, prediction accuracy is evaluated using the RMSE normalized by the range of the high-fidelity reference response (NRMSE):

$$\mathrm{NRMSE} = \frac{\sqrt{\dfrac{1}{N}\displaystyle\sum_{k=1}^{N}\left(\hat{y}_k - y_k\right)^2}}{y_{\max} - y_{\min}} \times 100\%, \tag{63}$$

$$y_{\max} = \max_{1\le k\le N} y_k, \qquad y_{\min} = \min_{1\le k\le N} y_k,$$

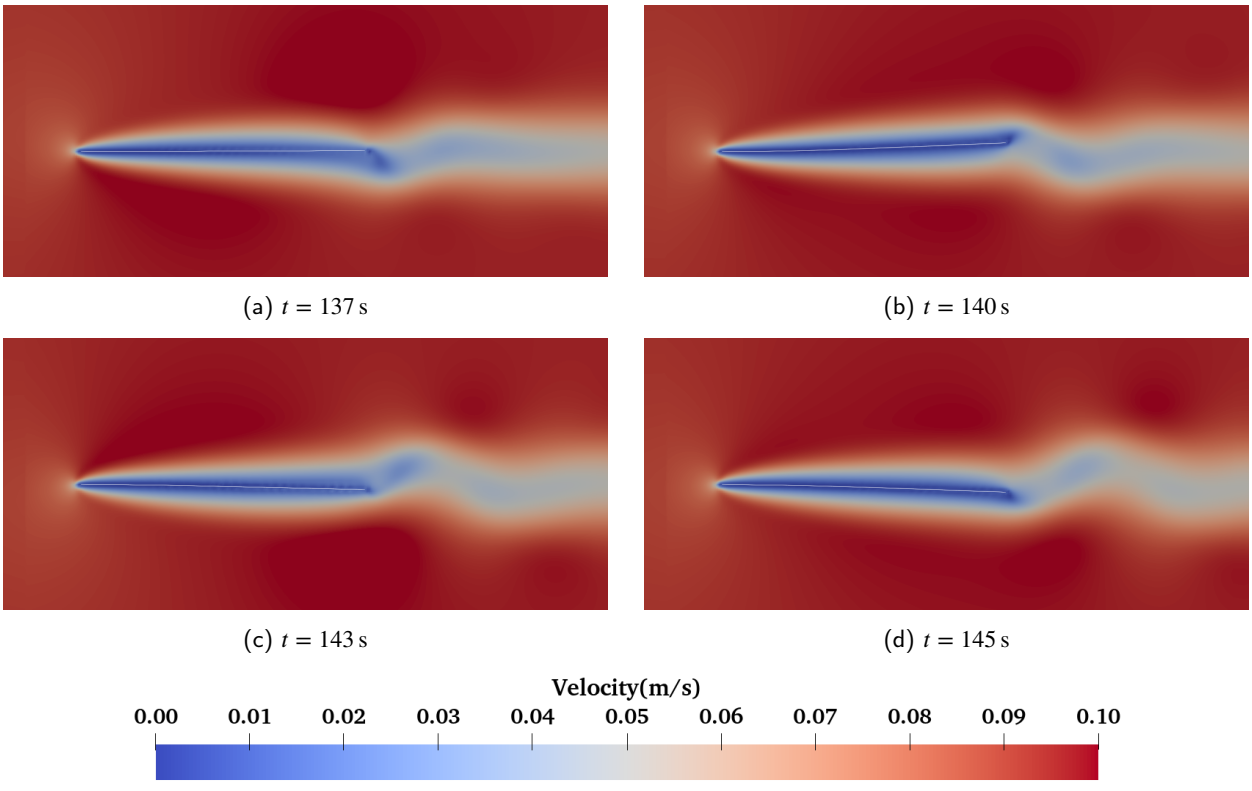


Figure 9: Velocity fields at representative instants during the frequency-sweep test: (a) 137 s; (b) 140 s; (c) 143 s; (d) 145 s.

where $\hat{y}_k$ and y_k are the predicted and high-fidelity reference values, respectively, and N is the number of evaluation samples after excluding the initial instant. The values $y_{\max}$ and $y_{\min}$ are the maximum and minimum of the reference response over the same evaluation interval. This metric measures the prediction RMSE relative to the range of the reference response; lower values indicate higher accuracy. For each response component in a given case, all methods use the same reference range for normalization. The initial state at 115 s is excluded, and the 560 samples from 115.0625 to 150 s are used for evaluation. The results are listed in Table 3.

Table 3
NRMSE (%) of the predicted responses under frequency-sweep excitation.

Method	F_x	F_y	M_z	Wingtip displacement
DMDc	22.52	7.99	6.94	7.18
DMDc+GPR	11.51	6.64	5.21	2.02
Hankel-DMDc	35.29	7.41	4.54	2.88
cOptDMDc	161.88	11.69	8.71	4.12
LC-DMDc	6.20	3.74	2.06	0.91

As shown in Table 3, LC-DMDc has the lowest full-interval prediction error for all four responses, with NRMSE values of 6.20%, 3.74%, 2.06%, and 0.91% for the streamwise force, transverse force, aerodynamic moment, and wingtip displacement, respectively. Relative to the best-performing comparison method for each response, the corresponding errors are reduced by 46.2%, 43.7%, 54.6%, and 55.1%. Thus, for this frequency-sweep case, LC-DMDc improves both aerodynamic load and structural displacement predictions, outperforming the comparison methods for all four responses.

Over the continuous 35 s rollout comprising 560 steps, LC-DMDc accurately preserves the main amplitudes and evolution of the aerodynamic loads and structural displacement under the frequency-sweep input, while achieving the

lowest full-interval error for every evaluated component. These results demonstrate its advantage in long-term response prediction for this frequency-sweep case and provide a basis for the subsequent evaluations under other input types.

4.1.2. Response predictions under piecewise sinusoidal inputs

Piecewise sinusoidal voltage inputs are used to compare the models under sustained periodic excitation and frequency changes. The input signal, shown in Figure 10, is defined as

$$V(t) = \begin{cases} A\, w(t - t_j) \sin\left[2\pi f_j (t - t_j)\right], & t_j < t < t_j + T, \quad j = 1, 2, 3, \\ 0, & \text{otherwise}, \end{cases} \tag{64}$$

where $A = 1200\,\text{V}$ and each segment has a duration of $T = 40\,\text{s}$. The start times and frequencies of the three segments are

$$\begin{aligned} (t_1, t_2, t_3) &= (10, 55, 100)\,\text{s}, \\ (f_1, f_2, f_3) &= (0.1, 0.2, 0.3)\,\text{Hz}. \end{aligned} \tag{65}$$

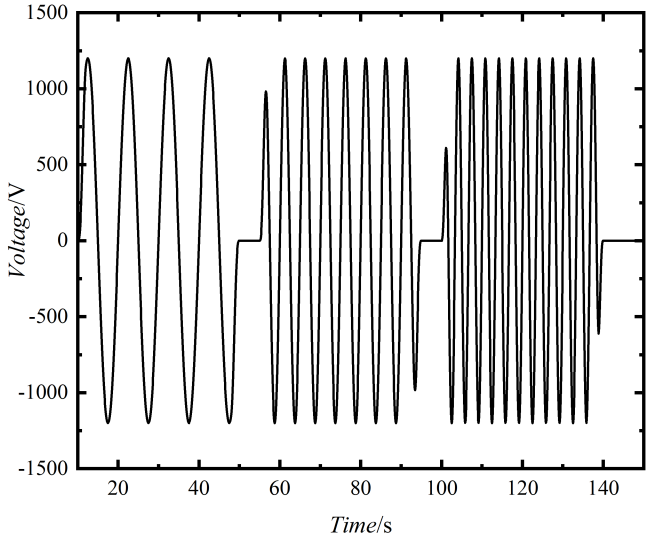


Figure 10: Piecewise constant-frequency sinusoidal voltage input.

The envelope w has the same half-cosine form as in Eq. (62), with the segment duration set to 40 s and transition durations of 2 s at both ends. Adjacent excitation segments are separated by 5 s intervals of zero voltage, and 140–150 s is the free-response interval. Each model starts from the initial state at 10 s and performs a continuous rollout to 150 s. Figure 11 compares the predicted streamwise aerodynamic force, transverse aerodynamic force, aerodynamic moment, and transverse wingtip displacement.

For the streamwise aerodynamic force F_x, standard DMDc predicts a mean load close to the reference but does not adequately capture the pronounced fluctuations during the first excitation segment. DMDc+GPR improves the prediction of some fluctuations but introduces additional oscillations in later segments, while Hankel-DMDc deviates from the reference in fluctuation amplitude and timing over some intervals. cOptDMDc produces excessively large streamwise force oscillations, indicating that the imposed stability constraint does not guarantee accurate load trajectories in this case. By contrast, LC-DMDc reproduces the changes in load fluctuation intensity across the excitation segments, with a full-interval streamwise force RMSE of 0.0200 mN, 69.3% lower than that of DMDc and 66.6% lower than that of DMDc+GPR.

The transverse aerodynamic force F_y and aerodynamic moment M_z further reveal differences in the predicted response amplitudes. During the 0.10 Hz excitation segment, standard DMDc substantially underestimates the main peaks and troughs, whereas cOptDMDc overestimates the amplitudes and shifts the peak timing in some cycles. DMDc+GPR and Hankel-DMDc improve on standard DMDc during this segment, but local waveform deviations

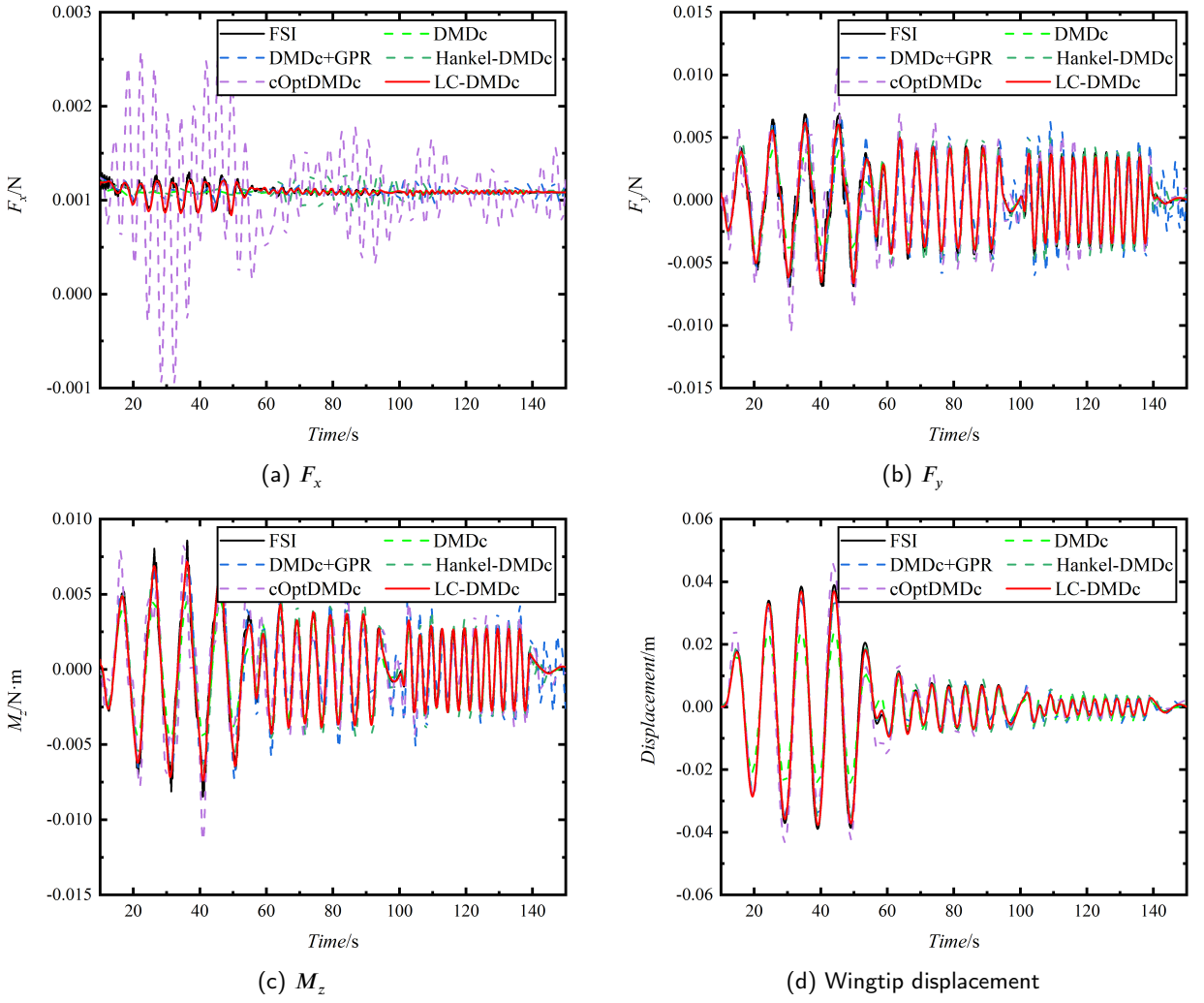


Figure 11: Aerodynamic and structural responses under piecewise sinusoidal excitation: (a) F_x; (b) F_y; (c) M_z; (d) transverse wingtip displacement. FSI denotes the high-fidelity reference solution.

remain after subsequent frequency changes. LC-DMDc captures the main oscillation amplitudes and their variations across the excitation conditions more accurately. Its full-interval RMSE values for the transverse force and aerodynamic moment are 0.433 mN and 0.284 mN m, respectively, representing reductions of 44.3% and 60.6% relative to Hankel-DMDc, the best-performing comparison method for both responses.

For structural displacement, the improvement provided by LC-DMDc is particularly pronounced for large-amplitude motion under low-frequency excitation. At approximately 44.06 s, the reference transverse wingtip displacement reaches 38.96 mm. Standard DMDc predicts a corresponding peak of only about 23.81 mm, whereas cOptDMDc overestimates it at approximately 45.73 mm. LC-DMDc predicts a peak of 36.92 mm, with peak timing consistent with the reference. It also follows the decrease in displacement amplitude during the subsequent two excitation segments. In particular, during the 0.30 Hz segment from 100 to 140 s, its wingtip displacement RMSE is only 0.126 mm, demonstrating that the same model can describe both large deformations at low frequencies and small-amplitude motion at higher frequencies.

The response after removal of the control input also reflects the models' ability to predict continuously. After the voltage returns to zero at 140 s, the high-fidelity solution shows a gradual decay in structural motion and load fluctuations. LC-DMDc follows this decay closely, whereas DMDc+GPR retains noticeable additional oscillations in the transverse force and moment. Over 140–150 s, the transverse force and moment RMSE values of LC-DMDc

are 0.0915 mN and 0.0665 mN m, respectively. Its predictive advantage therefore extends from the forced-vibration stage to the response evolution after removal of the control input. The range-normalized RMSE defined in Eq. (63) is evaluated using all 2240 prediction samples after excluding the initial instant, with the results listed in Table 4.

Table 4
NRMSE (%) of the predicted responses under piecewise sinusoidal excitation.

Method	F_x	F_y	M_z	Wingtip displacement
DMDc	14.77	6.74	5.52	6.27
DMDc+GPR	13.56	8.55	6.53	2.39
Hankel-DMDc	21.32	5.64	4.22	2.72
cOptDMDc	123.82	11.82	8.57	4.97
LC-DMDc	4.53	3.14	1.66	1.13

As shown in Table 4, LC-DMDc has the lowest full-interval prediction error for all four responses, with NRMSE values of 4.53%, 3.14%, 1.66%, and 1.13% for the streamwise force, transverse force, aerodynamic moment, and wingtip displacement, respectively. Relative to the best-performing comparison method for each response, the corresponding errors are reduced by 66.6%, 44.3%, 60.6%, and 52.9%. Thus, without reidentification, LC-DMDc applies the dynamics learned from the frequency-sweep data to the piecewise constant-frequency sinusoidal case and achieves the lowest full-interval prediction errors over a continuous 140 s rollout comprising 2240 steps. These results show that LC-DMDc accurately describes the aerodynamic loads and structural motion at different excitation frequencies, as well as the response changes following frequency transitions and input removal, demonstrating its ability to predict long-term responses across input types within the training frequency band.

4.1.3. Response predictions under multisine inputs

Multisine voltage inputs are used to evaluate the models' ability to predict aerodynamic loads and structural displacement under simultaneous excitation at multiple frequencies. Unlike the preceding frequency-sweep and piecewise constant-frequency sinusoidal cases, the multisine input superimposes several frequency components, producing a multifrequency response under sustained excitation. The input signal, shown in Figure 12, is defined as

$$V(t)=\begin{cases} A\,w(\tau)\displaystyle\sum_{j=1}^{4}\sin\left(2\pi f_j\tau+\phi_j\right), & 10\,\mathrm{s}<t<130\,\mathrm{s},\\ 0, & \text{otherwise,}\end{cases}\qquad \tau=t-10\,\mathrm{s}. \tag{66}$$

Each sinusoidal component has an amplitude of $A = 300\,\mathrm{V}$, with frequencies and initial phases given by

$$\begin{aligned}&(f_1,f_2,f_3,f_4)=(0.05,0.10,0.20,0.30)\,\mathrm{Hz},\\ &(\phi_1,\phi_2,\phi_3,\phi_4)=\left(0,\frac{\pi}{2},\pi,\frac{3\pi}{2}\right).\end{aligned} \tag{67}$$

The envelope w has the same half-cosine form as in Eq. (62), with an excitation duration of 120 s and transition durations of 2 s at both ends. The voltage returns to zero at 130 s, and the predictions continue to 150 s to examine the subsequent free response. Each model starts from the initial state at 10 s and performs a continuous rollout to 150 s. Figure 13 compares the predicted streamwise aerodynamic force, transverse aerodynamic force, aerodynamic moment, and transverse wingtip displacement.

The streamwise aerodynamic force F_x exhibits small fluctuations about a mean of approximately 1.088 mN, with a reference standard deviation of only about 0.02245 mN. Standard DMDc maintains the mean level but does not adequately capture local fluctuations. DMDc+GPR and Hankel-DMDc produce excessive fluctuations over some intervals, while the additional oscillations in cOptDMDc are more pronounced. LC-DMDc yields a full-interval streamwise force RMSE of 0.0113 mN, 44.0% lower than that of DMDc, the best-performing comparison method for this component. Its RMSE is approximately 0.0056 mN in each of the later intervals, 70–110 s and 110–130 s, indicating that it continues to track small load variations accurately after sustained rollout.

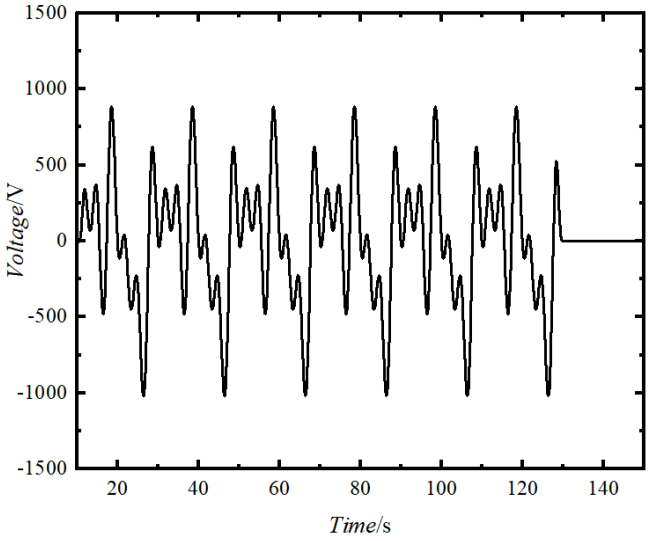


Figure 12: Multisine voltage input.

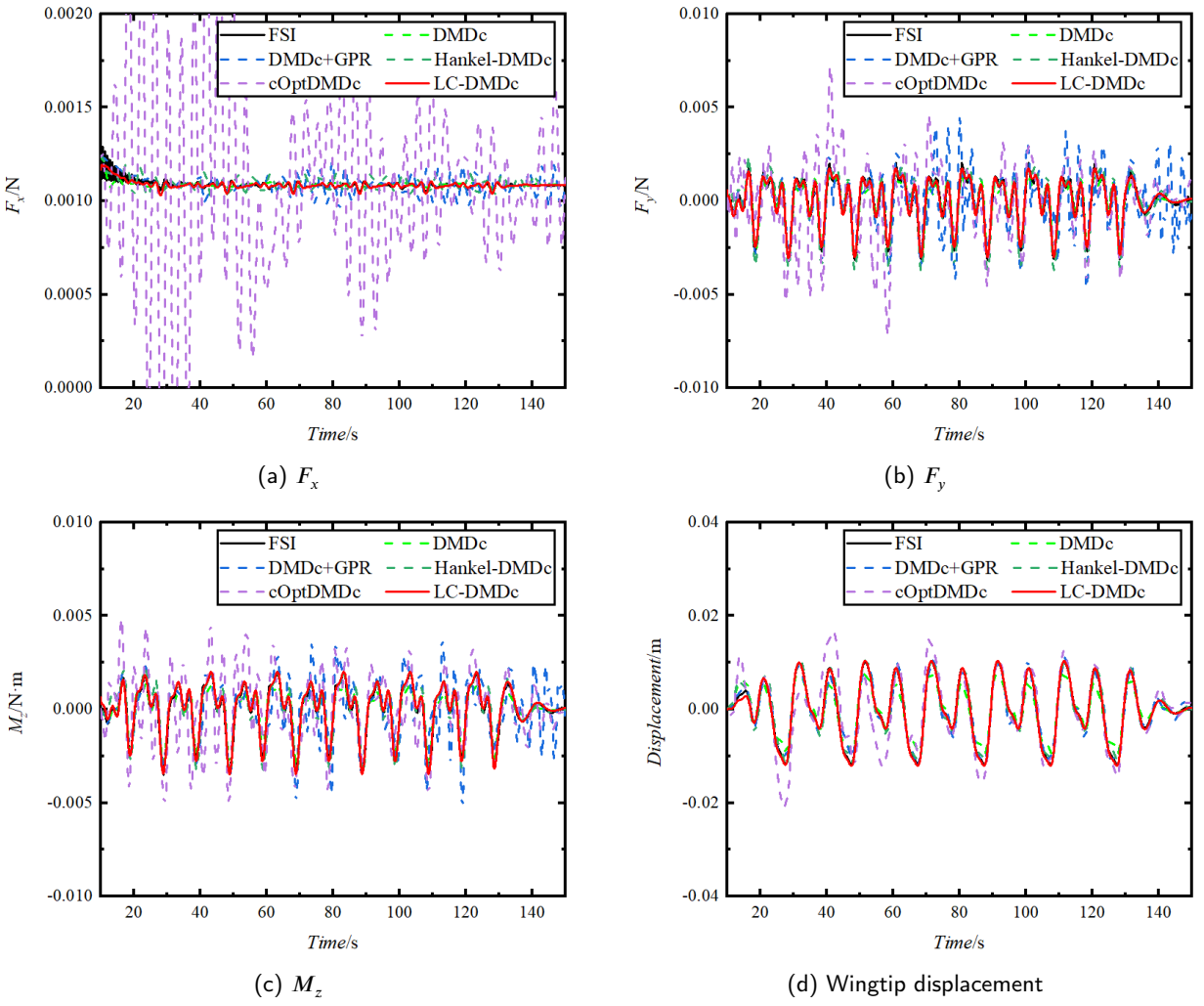
The transverse aerodynamic force F_y and aerodynamic moment M_z further show that improving predictions of some states does not necessarily improve all mechanical outputs. Although DMDc+GPR has a lower wingtip displacement error than standard DMDc, additional oscillations in its transverse force and moment predictions increase the full-interval errors for both outputs. Hankel-DMDc follows the timing of the main oscillations well but retains amplitude deviations at some peaks and troughs. The transverse force and moment RMSE values of LC-DMDc are 0.140 mN and 0.118 mN m, respectively, 45.6% and 64.0% lower than those of DMDc, the best-performing comparison method for both outputs.

For structural displacement, LC-DMDc accurately preserves the amplitudes and trough timing of the multifrequency response. For example, near the negative displacement peak at approximately 67.5 s, the high-fidelity result is about -11.82 mm, compared with approximately -9.39 mm for standard DMDc and -12.06 mm for LC-DMDc. The LC-DMDc peak timing differs from the reference by only one sampling interval, 0.0625 s. Over the full trajectory, its wingtip displacement RMSE is 0.268 mm, 84.8% lower than that of DMDc and 73.9% lower than that of Hankel-DMDc, the best-performing comparison method for displacement. Thus, LC-DMDc improves aerodynamic load prediction without sacrificing structural motion accuracy, improving both predictions simultaneously. The previously defined NRMSE in Eq. (63) is evaluated using all 2240 prediction samples after excluding the initial instant. The results are listed in Table 5.

Table 5
NRMSE (%) of the predicted responses under multisine excitation.

Method	F_x	F_y	M_z	Wingtip displacement
DMDc	8.51	4.87	5.98	8.07
DMDc+GPR	20.21	19.92	18.70	5.33
Hankel-DMDc	16.36	7.13	6.32	4.70
cOptDMDc	230.95	29.83	26.64	17.24
LC-DMDc	4.77	2.65	2.15	1.23

As shown in Table 5, LC-DMDc has the lowest full-interval prediction error for all four responses, with NRMSE values of 4.77%, 2.65%, 2.15%, and 1.23% for the streamwise force, transverse force, aerodynamic moment, and wingtip displacement, respectively. Relative to the best-performing comparison method for each response, the corresponding errors are reduced by 44.0%, 45.6%, 64.0%, and 73.9%. These results show that LC-DMDc simultaneously improves aerodynamic load and structural displacement predictions under excitation at multiple frequencies.



(a) F_x (b) F_y

(c) M_z (d) Wingtip displacement

Figure 13: Aerodynamic and structural responses under multisine excitation: (a) F_x; (b) F_y; (c) M_z; (d) transverse wingtip displacement. FSI denotes the high-fidelity reference solution.

Over the continuous 140 s rollout comprising 2240 steps, LC-DMDc accurately reproduces the aerodynamic loads and structural displacement under simultaneous multifrequency excitation, maintaining low errors during both the sustained forced response and the subsequent free response. These results indicate that LC-DMDc identified from frequency-sweep data can predict responses to multisine inputs within the training frequency band, accurately describing both aerodynamic loads and structural motion without reidentification.

4.1.4. Response predictions under step inputs

Smooth step pulses of alternating polarity are used to evaluate the models during loading, constant-voltage holding, unloading, and actuation reversal. Unlike the preceding oscillatory inputs, this case contains sustained constant-voltage intervals, testing the models' ability to describe sustained structural deformation and load transitions. The input signal, shown in Figure 14, is defined as

$$V(t) = \sum_{j=1}^{4} A_j \, w(t - t_j), \tag{68}$$

where the start times and amplitudes of the four pulses are

$$\begin{aligned}(t_1, t_2, t_3, t_4) &= (10, 45, 80, 115)\,\mathrm{s},\\ (A_1, A_2, A_3, A_4) &= (1000, -1000, 1000, -1000)\,\mathrm{V}.\end{aligned} \tag{69}$$

Each pulse lasts $T = 25\,\mathrm{s}$, comprising 5 s of smooth loading, 15 s at constant voltage, and 5 s of smooth unloading. The corresponding envelope is

$$w(\tau) = \begin{cases} \dfrac{1 - \cos(\pi\tau/T_\mathrm{r})}{2}, & 0 \le \tau < T_\mathrm{r},\\ 1, & T_\mathrm{r} \le \tau \le T - T_\mathrm{r},\\ \dfrac{1 - \cos\left[\pi(T-\tau)/T_\mathrm{r}\right]}{2}, & T - T_\mathrm{r} < \tau \le T,\\ 0, & \text{otherwise}, \end{cases} \tag{70}$$

where $T_\mathrm{r} = 5\,\mathrm{s}$ and $\tau = t - t_j$ is the time elapsed since the start of pulse j.

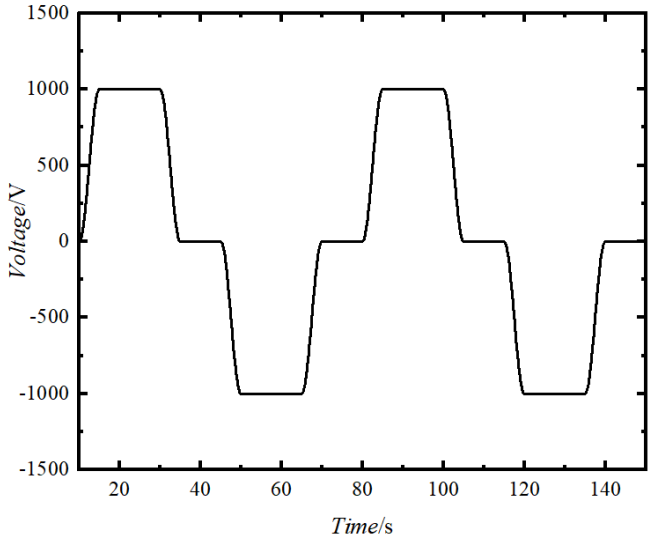


Figure 14: Smooth step voltage pulses of alternating polarity.

The voltage is zero between pulses, and 140–150 s is the free-response interval after the final unloading. Each model starts from the initial state at 10 s and performs a continuous rollout to 150 s. Figure 15 compares the predicted streamwise aerodynamic force, transverse aerodynamic force, aerodynamic moment, and transverse wingtip displacement.

Among all responses, structural displacement shows the most pronounced improvement. Standard DMDc underestimates both the displacement peaks following loading and the deformation maintained under constant voltage. For example, during 20–30 s of the first positive-voltage plateau, the reference mean wingtip displacement is approximately 12.15 mm, whereas standard DMDc predicts only about 5.65 mm and LC-DMDc predicts approximately 12.31 mm. During 55–65 s of the subsequent negative-voltage plateau, the reference mean displacement is about −12.17 mm, compared with approximately −5.72 mm for DMDc and −12.29 mm for LC-DMDc. The results for both polarities show that LC-DMDc accurately maintains the structural deformation level under sustained actuation. It also reproduces the displacement peaks and their timing during loading transients. For example, following the positive loading phase of the third pulse, the reference wingtip displacement reaches 17.41 mm at approximately 87.38 s. The corresponding peaks predicted by standard DMDc and LC-DMDc are about 11.32 mm and 17.29 mm, respectively, with the LC-DMDc peak timing differing from the reference by only one sampling interval, 0.0625 s. DMDc+GPR and Hankel-DMDc reduce the displacement amplitude underestimation of standard DMDc, but deviations remain over the full trajectory.

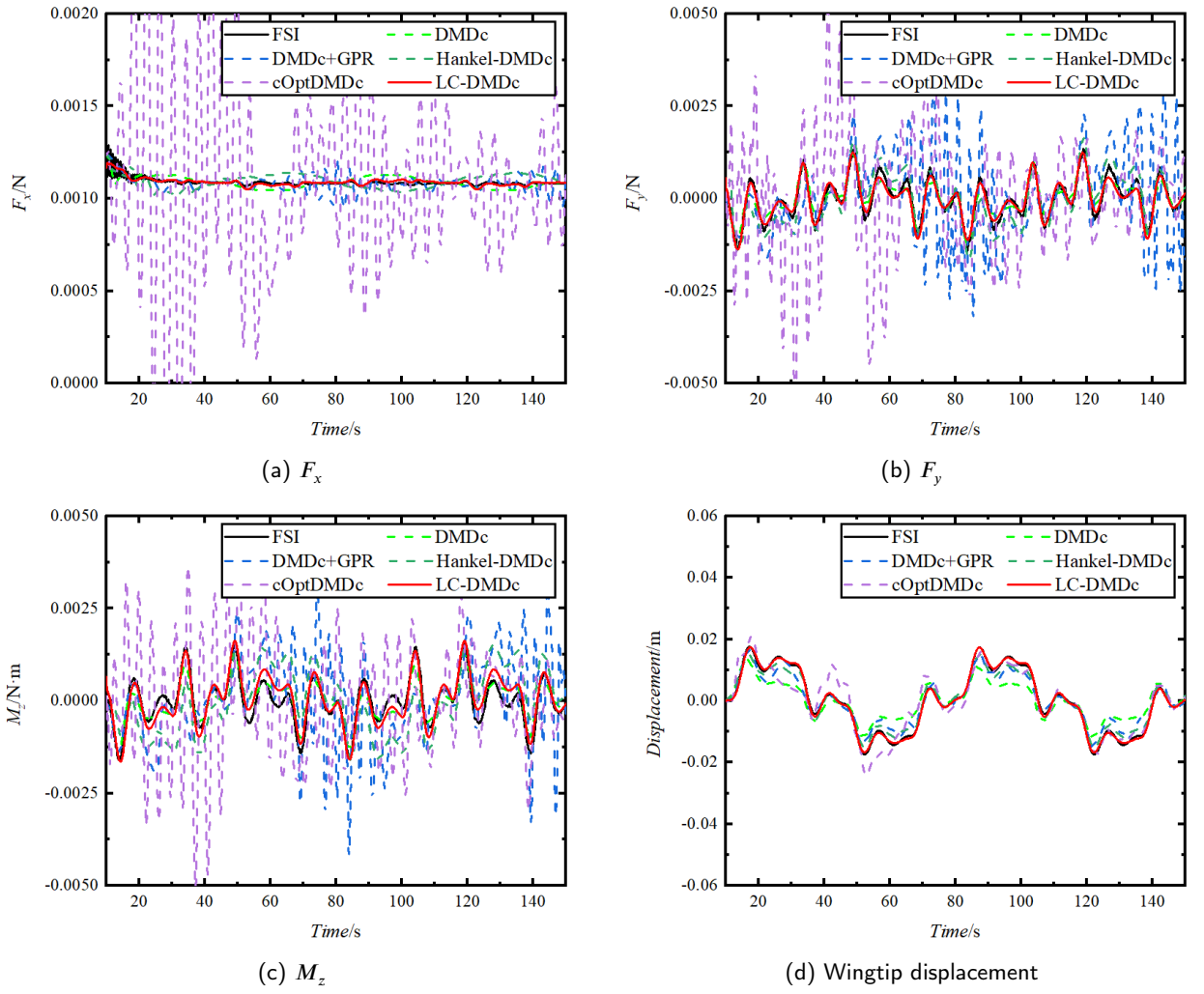


Figure 15: Aerodynamic and structural responses under step excitation: (a) F_x; (b) F_y; (c) M_z; (d) transverse wingtip displacement. FSI denotes the high-fidelity reference solution.

The wingtip displacement RMSE of LC-DMDc is 0.437 mm, 90.9% lower than that of DMDc and 75.1% lower than that of Hankel-DMDc, the best-performing comparison method for displacement.

The streamwise aerodynamic force F_x exhibits small variations about its mean. Standard DMDc, DMDc+GPR, and Hankel-DMDc maintain broadly similar load levels but retain errors in local variations, whereas cOptDMDc produces excessively large additional oscillations. LC-DMDc yields a full-interval streamwise force RMSE of 0.0122 mN, 58.1% lower than that of DMDc, the best-performing comparison method for this component. For the transverse aerodynamic force, LC-DMDc captures the main peaks and troughs associated with loading, unloading, and actuation reversal, with an RMSE of 0.125 mN, 29.3% lower than that of DMDc. By comparison, DMDc+GPR and cOptDMDc introduce pronounced oscillations absent from the reference over some intervals, while Hankel-DMDc shows deviations in amplitude or response level at some stages.

The prediction results for the aerodynamic moment M_z differ from those for displacement and aerodynamic forces. LC-DMDc and standard DMDc both capture the main variations, with similar full-interval RMSE values of 0.230 and 0.232 mN m, respectively. During the second and fourth negative pulses, LC-DMDc has a slightly higher moment error than standard DMDc. Thus, in the step-input case, the main improvements from LC-DMDc are in structural displacement and aerodynamic force prediction. Its moment prediction is comparable to that of standard DMDc but remains more accurate than those of the other three comparison methods.

The results after unloading further test the models' ability to describe the free response. After the voltage returns to zero at 140 s, LC-DMDc follows the gradual decay of structural displacement and transverse load fluctuations. Over 140–150 s, its transverse force, aerodynamic moment, and wingtip displacement RMSE values are 0.0903 mN, 0.106 mN m, and 0.213 mm, respectively, all lower than those of the comparison methods. These results show that the improvement in controlled-response prediction extends from constant-voltage actuation to the motion after removal of the control input. The previously defined NRMSE in Eq. (63) is evaluated using all 2240 prediction samples after excluding the initial instant. The results are listed in Table 6.

Table 6
NRMSE (%) of the predicted responses under step excitation.

Method	F_x	F_y	M_z	Wingtip displacement
DMDc	12.93	6.42	7.39	13.78
DMDc+GPR	17.52	36.27	35.27	7.20
Hankel-DMDc	17.93	12.13	25.29	5.01
cOptDMDc	241.29	56.36	46.52	10.96
LC-DMDc	5.42	4.54	7.33	1.25

As shown in Table 6, LC-DMDc has the lowest NRMSE for all four responses, with values of 5.42%, 4.54%, 7.33%, and 1.25% for the streamwise force, transverse force, aerodynamic moment, and wingtip displacement, respectively. Relative to the best-performing comparison method for each response, the streamwise force, transverse force, and wingtip displacement errors are reduced by 58.1%, 29.3%, and 75.1%, respectively. The moment error decreases by only about 0.85%, remaining comparable to that of standard DMDc. Thus, the main advantages of LC-DMDc in this case are its accurate description of structural deformation under sustained actuation and improved aerodynamic force prediction during loading, unloading, and actuation reversal; further improvement in moment prediction remains possible.

Without reidentification, LC-DMDc applies the dynamics learned from frequency-sweep data to step inputs with constant-voltage holding and polarity reversals, accurately reproducing loading, sustained deformation, and unloading over a 140 s rollout comprising 2240 steps. These results further show that LC-DMDc accommodates different control input types, substantially improving the overall accuracy of aerodynamic force and structural displacement predictions while maintaining moment prediction accuracy.

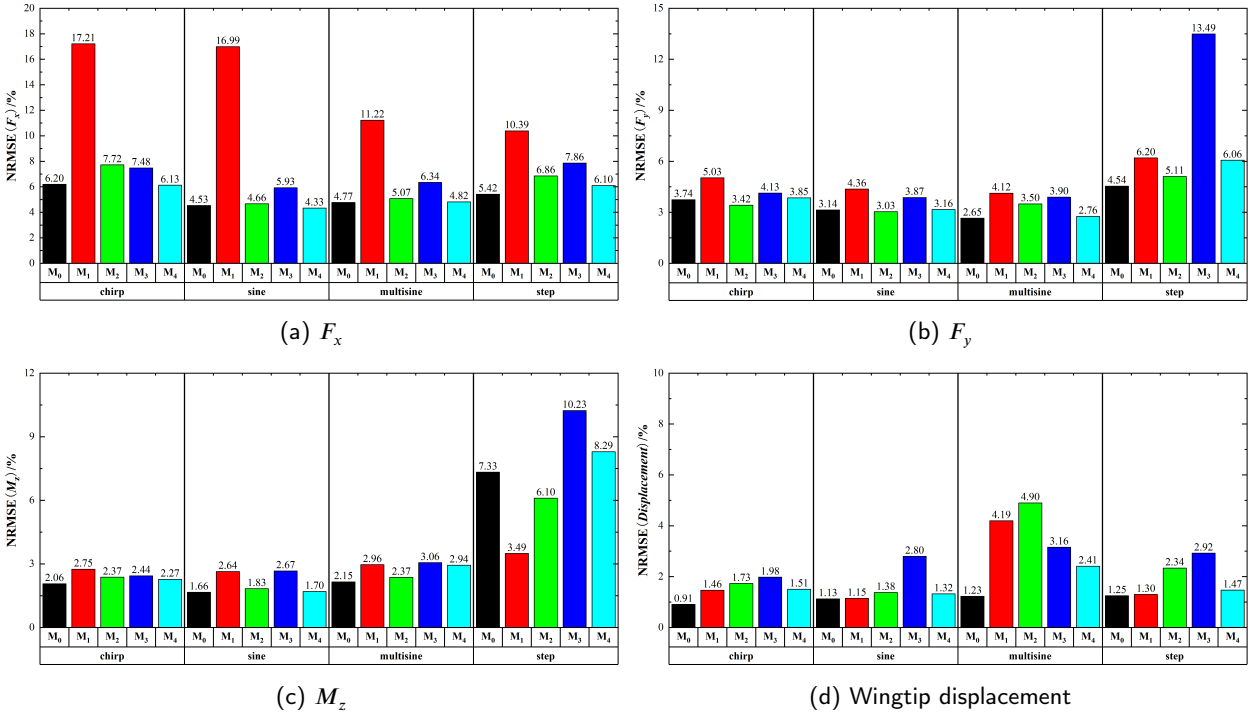
4.2. Effects of key components on prediction accuracy

Ablation studies under frequency-sweep, piecewise constant-frequency sinusoidal, multisine, and step inputs assess the contribution of each LC-DMDc component to prediction performance. With the full model M_0 as the baseline, the variants separately remove the nonlinear RBF features, displacement–velocity kinematic constraint, or auxiliary power loss, or change the training rollout horizon, as listed in Table 7. All variants use the same training data and POD bases. Each ablated model is reidentified with the same maximum number of optimization iterations, while the full model from Section 4.1 is retained to provide a consistent evaluation baseline.

Table 7
Model configurations for the ablation study.

Model	Configuration
M_0	Full LC-DMDc model
M_1	Remove RBF features; retain only the state, control input, and constant term in the load mapping
M_2	Remove the displacement–velocity kinematic constraint; fit the corresponding state components by unconstrained regression
M_3	Train using only 64-step prediction errors
M_4	Remove the auxiliary power loss
M_5	Train using only one-step prediction errors

Figure 16 compares the prediction errors of M_0–M_4 in the four cases using the previously defined range-normalized RMSE in Eq. (63). In all four cases, M_5 reaches the numerical divergence threshold approximately 1.1–1.2 s after prediction begins, so its NRMSE is not plotted. The other variants, all trained using multistep prediction errors, complete the entire test interval. Under the present model configuration and training conditions, these results indicate that incorporating errors from continuous rollouts into identification is important for sustaining long-term predictions.



(a) F_x (b) F_y

(c) M_z (d) Wingtip displacement

Figure 16: NRMSE of models M_0–M_4 under four input types: (a) F_x; (b) F_y; (c) M_z; (d) transverse wingtip displacement. The labels "chirp" and "sine" denote frequency-sweep and piecewise constant-frequency sinusoidal inputs, respectively.

Under frequency-sweep excitation, the full model M_0 has NRMSE values of 6.20%, 3.74%, 2.06%, and 0.91% for the streamwise force, transverse force, aerodynamic moment, and wingtip displacement, respectively. Removing RBF features in M_1 increases these errors to 17.21%, 5.03%, 2.75%, and 1.46%, with the largest increase in the streamwise force error. The full model reduces this error by 64.0% relative to M_1. Thus, when the excitation frequency varies continuously, an affine load mapping alone does not achieve the accuracy of the full model, and nonlinear RBF features improve the predictions of aerodynamic forces, moments, and structural responses. Removing the kinematic constraint in M_2 increases the wingtip displacement error to 1.73% and also increases the streamwise force and moment errors, although the transverse force error decreases slightly to 3.42%. Model M_3, trained using only 64-step prediction errors, performs worse than the full model for all four metrics, with a displacement error of 1.98%. Removing the auxiliary power loss in M_4 mainly increases the moment and displacement errors, to 2.27% and 1.51%, respectively. For frequency-sweep excitation, the nonlinear load mapping therefore provides a particularly pronounced improvement in streamwise force prediction, while the kinematic constraint, longer training horizon, and auxiliary power loss all improve structural response accuracy.

Under piecewise constant-frequency sinusoidal excitation, the streamwise force, transverse force, moment, and displacement errors of M_0 are 4.53%, 3.14%, 1.66%, and 1.13%, respectively. Removing RBF features increases the first three errors in M_1 to 16.99%, 4.36%, and 2.64%, whereas the displacement error increases only slightly, to 1.15%. This indicates that RBF features primarily improve aerodynamic force and moment prediction in this case: similar structural displacement errors can coexist with substantial differences in load prediction accuracy. Without the kinematic constraint, the moment and displacement errors of M_2 increase to 1.83% and 1.38%, respectively, while the transverse force error decreases slightly. By comparison, shortening the training horizon has a more pronounced effect on sustained oscillation prediction. The moment and displacement errors of M_3 reach 2.67% and 2.80%, respectively;

the full model reduces these errors by 37.6% and 59.7%. The moment error of M_4 is 1.70%, close to that of the full model, but its displacement error increases to 1.32%. Thus, the nonlinear load mapping mainly improves aerodynamic force prediction in this case, whereas a longer training horizon has a more pronounced effect on structural oscillation and moment predictions.

Under multisine excitation, the full model outperforms every ablated variant for all four metrics. The streamwise force, transverse force, moment, and displacement errors of M_0 are 4.77%, 2.65%, 2.15%, and 1.23%, respectively; removing RBF features increases them to 11.22%, 4.12%, 2.96%, and 4.19%. Relative to M_1, the full model reduces the streamwise force and displacement errors by 57.5% and 70.8%, respectively, indicating that the nonlinear load mapping is important for predicting both aerodynamic forces and structural motion under simultaneous multifrequency excitation. Removing the kinematic constraint increases the displacement error of M_2 to 4.90%, approximately four times that of the full model, and the transverse force error to 3.50%. This indicates that preserving the displacement–velocity relation improves the accuracy of multifrequency structural response predictions and the corresponding loads. All four errors increase in M_3, including a displacement error of 3.16%, further demonstrating the benefit of a longer training horizon. Removing the auxiliary power loss in M_4 has little effect on the streamwise and transverse force errors, but increases the moment and displacement errors to 2.94% and 2.41%, respectively. Compared with the preceding two cases, the benefits of the individual components are more consistent under multisine excitation.

The step input includes loading, holding, and unloading stages, allowing the models to be assessed during input transitions and the subsequent response. The streamwise force, transverse force, moment, and displacement errors of M_0 are 5.42%, 4.54%, 7.33%, and 1.25%, respectively. Removing RBF features in M_1 increases the streamwise and transverse force errors to 10.39% and 6.20% and slightly increases the displacement error to 1.30%, but reduces the moment error to 3.49%. Removing the kinematic constraint in M_2 produces a similar pattern: the streamwise force, transverse force, and displacement errors increase to 6.86%, 5.11%, and 2.34%, respectively, while the moment error decreases to 6.10%. Thus, the nonlinear mapping and kinematic constraint improve force and displacement predictions in this case but do not reduce the moment error. The effect of the training horizon is more consistent: all four errors in M_3 exceed those of the full model, with transverse force and displacement errors of 13.49% and 2.92%, respectively. Including 256-step prediction errors reduces these two errors by 66.4% and 57.3%, indicating that a longer training horizon reduces deviations in the subsequent response to step inputs. All four errors in M_4 also exceed those of the full model, showing that the auxiliary power loss further improves predictions in this loading–unloading case.

Across all four cases, the nonlinear RBF load mapping reduces the streamwise and transverse force prediction errors by 47.8%–73.3% and 25.6%–35.8%, respectively, relative to the variant without RBF features. Its improvement in structural displacement prediction is most pronounced in the multisine case. The kinematic constraint improves wingtip displacement accuracy in all four cases and is particularly beneficial for describing structural motion under simultaneous multifrequency excitation. Multistep training enables the present model to sustain continuous rollouts. Adding a longer training horizon further reduces the errors of all response components in every case, with a particularly pronounced improvement in transverse force prediction under step inputs. The auxiliary power loss mainly improves structural displacement and selected mechanical outputs. These results indicate that the components contribute through nonlinear representation, structural kinematics, and control of rollout errors, together improving the long-term prediction performance of LC-DMDc under different control inputs.

5. Conclusions

This study proposes load-coupled dynamic mode decomposition with control (LC-DMDc) to address the difficulty of representing nonlinear aerodynamic loads with compact linear models and the accumulation of prediction errors during long rollouts in controlled FSI systems. LC-DMDc introduces radial basis functions into the DMDc framework to construct a nonlinear load mapping, with shared low-dimensional load coefficients linking state evolution and mechanical outputs. It preserves the displacement–velocity kinematic relation and improves long-term prediction accuracy through joint multistep training. A high-fidelity FSI solver for a piezoelectrically actuated flat-plate airfoil was developed using OpenFOAM, a multi-direct-forcing immersed boundary method, and an Euler–Bernoulli beam model, with implicit fluid–structure coupling implemented through preCICE. Response data under frequency-sweep excitation were then used to train the reduced-order model. Comparisons with DMDc, DMDc+GPR, Hankel-DMDc, and cOptDMDc under frequency-sweep, piecewise constant-frequency sinusoidal, multisine, and step inputs validate the accuracy of LC-DMDc.

The results show that LC-DMDc maintains good accuracy in predicting aerodynamic loads and structural responses over continuous rollouts under different inputs. Across all four cases, the streamwise force, transverse force, aerodynamic moment, and wingtip displacement errors do not exceed 6.20%, 4.54%, 7.33%, and 1.25%, respectively. The ablation studies further clarify the contributions of the individual components. First, the nonlinear RBF load mapping improves the representation of aerodynamic load variations. Compared with the variant without RBF features, the full model reduces the streamwise and transverse force errors by 47.8%–73.3% and 25.6%–35.8%, respectively, across all four cases, and the displacement error by 70.8% in the multisine case. In addition to nonlinear modeling, incorporating multistep prediction errors into training is important for sustaining continuous rollouts. The model trained using only one-step prediction errors diverges numerically in all four cases. Adding 256-step prediction errors to 64-step training further reduces the errors of all response components in every case; under step excitation, the transverse force and displacement errors decrease by 66.4% and 57.3%, respectively. Furthermore, both the displacement–velocity kinematic constraint and the auxiliary power loss improve structural response prediction accuracy. In the multisine case, removing the kinematic constraint increases the displacement error from 1.23% to 4.90%, whereas removing the auxiliary power loss increases it to 2.41%. These results indicate that the nonlinear load mapping, joint multistep training, kinematic constraint, and auxiliary power loss improve prediction performance through nonlinear representation, control of errors during continuous rollouts, and preservation of structural kinematics. Together, these components enable LC-DMDc to predict long-term aerodynamic loads and structural responses under different control inputs.

Acknowledgments

This work was supported by the Basic Research Program (JCKY2024208A006) from the State Administration of Science, Technology and Industry for National Defense, the Civilian Space Program (D020101) from the State Administration of Science, Technology and Industry for National Defense, the Shanghai Spaceflight Innovation Fund Program (Grant No. SAST2025-025) and Natural Science Basic Research Program of Shaanxi Province (Grant No. 2025SYS-SYSZD-053). This work was also supported by HPC Platform from Xi'an Jiaotong University.

Declaration of competing interests

The authors declare that they have no competing interests.

References

[1] M. K. Hickner, U. Fasel, A. G. Nair, B. W. Brunton, S. L. Brunton, Data-Driven Unsteady Aeroelastic Modeling for Control, AIAA Journal 61 (2) (2023) 780–792. doi:10.2514/1.J061518.

[2] J. Bae, J. Lee, S. Kim, J. Ha, B.-S. Lee, Y. Park, C. Choong, J.-B. Kim, Z. L. Wang, H.-Y. Kim, J.-J. Park, U. I. Chung, Flutter-driven triboelectrification for harvesting wind energy, Nature Communications 5 (1) (2014). doi:10.1038/ncomms5929.

[3] Y. Wu, J. Li, Y. Dai, Y. Li, C. Yang, Active maneuver load alleviation for a pitching wing via spanwise-distributed camber morphing, Aerospace Science and Technology 155 (2024). doi:10.1016/j.ast.2024.109693.

[4] W. Gao, Y. Liu, Q. Li, B. Lu, Gust load alleviation of a flexible flying wing with linear parameter-varying modeling and model predictive control, Aerospace Science and Technology 155 (2024). doi:10.1016/j.ast.2024.109671.

[5] A. J. Russell, M. Collu, A. S. McDonald, P. R. Thies, A. Keane, A. R. Quayle, LIDAR-assisted feedforward individual pitch control of a 15 MW floating offshore wind turbine, Wind Energy 27 (4) (2024) 341–362. doi:10.1002/we.2891.

[6] J. Liu, C. Cai, D. Song, J. Zheng, X. Guo, X. Sun, Z. Hu, Q. Li, Power output and platform motion regulation of floating offshore wind turbine using model predictive control based on coupled dynamics model, Ocean Engineering 322 (2025). doi:10.1016/j.oceaneng.2025.120451.

[7] K. Iguchi, T. Shimooka, S. Uchikai, Y. Konno, H. Tanaka, Y. Ikemoto, J. Shintake, Agile robotic fish based on direct drive of continuum body, npj Robotics 2 (1) (2024). doi:10.1038/s44182-024-00014-z.

[8] T. He, W. Su, Robust control of gust-induced vibration of highly flexible aircraft, Aerospace Science and Technology 143 (2023). doi:10.1016/j.ast.2023.108703.

[9] E. H. W. Ang, B. F. Ng, Genetic algorithm LQG and neural network controllers for gust response alleviation of flying wing unmanned aerial vehicles, Journal of Fluids and Structures 130 (2024). doi:10.1016/j.jfluidstructs.2024.104199.

[10] C. Brown, G. McGowan, K. Cooley, J. Deese, T. Josey, E. H. Dowell, J. P. Thomas, Convolution/Volterra Reduced-Order Modeling for Nonlinear Aeroelastic Limit Cycle Oscillation Analysis and Control, AIAA Journal 60 (12) (2022) 6647–6664. doi:10.2514/1.J061845.

[11] M. Candon, E. Hale, M. Balajewicz, A. Delgado-Gutiérrez, V. Muscarello, P. Marzocca, Parameterization of nonlinear aeroelastic reduced order models via direct interpolation of Taylor partial derivatives, Nonlinear Dynamics 112 (20) (2024) 17649–17670. doi:10.1007/s11071-024-09976-z.

[12] J. Li, Y. Dai, Y. Hu, Y. Zhang, C. Yang, Deep reinforcement learning control for stall flutter via active camber morphing, Physics of Fluids 37 (10) (2025). doi:10.1063/5.0295770.

[13] L. Gkimisis, T. Richter, P. Benner, Adjacency-based, non-intrusive model reduction for vortex-induced vibrations, Computers & Fluids 275 (2024). doi:10.1016/j.compfluid.2024.106248.

[14] A. Prakash, Y. J. Zhang, Nonintrusive projection-based reduced order modeling using stable learned differential operators, Computer Methods in Applied Mechanics and Engineering 442 (2025). doi:10.1016/j.cma.2025.117946.

[15] E. Rezaian, C. Huang, K. Duraisamy, Non-intrusive balancing transformation of highly stiff systems with lightly damped impulse response, Philos Trans A Math Phys Eng Sci 380 (2229) (2022) 20210202. doi:10.1098/rsta.2021.0202.
URL https://www.ncbi.nlm.nih.gov/pubmed/35719076

[16] E. Rezaian, K. Duraisamy, Data-Driven Balanced Truncation for Predictive Model Order Reduction of Aeroacoustic Response, AIAA Journal 61 (10) (2023) 4524–4545. doi:10.2514/1.J063116.

[17] J. L. Proctor, S. L. Brunton, J. N. Kutz, Dynamic mode decomposition with control, SIAM Journal on Applied Dynamical Systems 15 (1) (2016) 142–161.

[18] P. J. Schmid, Dynamic Mode Decomposition and Its Variants, Annual Review of Fluid Mechanics 54 (1) (2022) 225–254. doi:10.1146/annurev-fluid-030121-015835.

[19] M. A. Gultekin, Z. Zhang, A. Bazzi, Dynamic Mode Decomposition for Real-Time System Estimation of Induction Motor Drives, IEEE Transactions on Industry Applications 59 (2) (2023) 1836–1848. doi:10.1109/tia.2022.3231843.

[20] M. Merino-Olagüe, J. Ibarrola-Chamizo, X. Iriarte, A. Plaza, Application of DMD family methods and Higher Order DMD with Control for Reduced-Order Modelling of Nonlinear Elastic Structures, Mathematics and Computers in Simulation 250 (2026) 866–882. doi:10.1016/j.matcom.2026.07.014.

[21] G. Immordino, A. Vaiuso, A. Da Ronch, M. Righi, Spatio-temporal graph convolutional autoencoder for transonic wing pressure distribution forecasting, Aerospace Science and Technology 165 (2025). doi:10.1016/j.ast.2025.110516.

[22] T. Wang, D. Li, K. Zhu, F. Cao, D. Greaves, M. Hann, H. Shi, Application of dynamic mode decomposition in floating offshore renewable energy systems: Nonlinear prediction, denoise and control separation, Energy 341 (2025). doi:10.1016/j.energy.2025.139270.

[23] G. Palma, A. Serani, S. Aram, D. W. Wundrow, D. Drazen, M. Diez, Model-free system identification of surface ships in waves via Hankel dynamic mode decomposition with control, Ocean Engineering 341 (2025). doi:10.1016/j.oceaneng.2025.122539.

[24] H. Namiki, A. Saito, Short-time dynamic mode decomposition: a data-driven forced response analysis of nonlinear systems under swept-sine excitation, Nonlinear Dynamics 113 (24) (2025) 33109–33126. doi:10.1007/s11071-025-11751-7.

[25] Y. Peng, J. Song, Z. Xie, B. Wang, W. Cai, D. Peng, Y. Liu, X. Wen, Kalman filter-based dynamic mode decomposition for closed-loop flow control with noise-corrupted sensing, Journal of Computational Physics 542 (2025). doi:10.1016/j.jcp.2025.114386.

[26] J. A. Rosenfeld, R. Kamalapurkar, Dynamic Mode Decomposition With Control Liouville Operators, IEEE Transactions on Automatic Control 69 (12) (2024) 8571–8586. doi:10.1109/tac.2024.3419179.

[27] X. Qian, H. Wu, J. Zhao, S. Jia, Y. Luo, X. Yuan, A fast data and mechanism fusion modeling method for dynamic absorption/distillation processes, Chemical Engineering Science 320 (2026). doi:10.1016/j.ces.2025.122607.

[28] Q. Ouyang, L. Dong, J. Liu, J. Zhou, A scaled derivative-based DMDc method for modelling multiple-input multiple-output mechanical systems, Applied Mathematical Modelling 140 (2025) 115866. doi:10.1016/j.apm.2024.115866.

[29] A. Tsolovikos, E. Bakolas, D. Goldstein, Dynamic Mode Decomposition With Gaussian Process Regression for Control of High-Dimensional Nonlinear Systems, Journal of Dynamic Systems, Measurement, and Control 146 (6) (2024). doi:10.1115/1.4065594.

[30] J. Rains, Y. Wang, A. House, A. L. Kaminsky, N. A. Tison, V. M. Korivi, Constrained optimized dynamic mode decomposition with control for physically stable systems with exogeneous inputs, Journal of Computational Physics 496 (2024). doi:10.1016/j.jcp.2023.112604.

[31] J. Rains, D. Huang, Y. Wang, Residual dynamic mode decomposition with control for nonlinear dynamic systems, Structural and Multidisciplinary Optimization 69 (2) (2026). doi:10.1007/s00158-025-04205-6.

[32] N. Fonzi, S. L. Brunton, U. Fasel, Data-driven nonlinear aeroelastic models of morphing wings for control, Proc Math Phys Eng Sci 476 (2239) (2020) 20200079. doi:10.1098/rspa.2020.0079.
URL https://www.ncbi.nlm.nih.gov/pubmed/32831607

[33] N. Fonzi, S. L. Brunton, U. Fasel, Data-Driven Modeling for Transonic Aeroelastic Analysis, Journal of Aircraft 61 (2) (2024) 625–637. doi:10.2514/1.C037409.

[34] X. Li, J. Deng, Active control of the flow past a circular cylinder using online dynamic mode decomposition, Journal of Fluid Mechanics 997 (2024). doi:10.1017/jfm.2024.738.

[35] A. K. Al-Jiboory, Adaptive quadrotor control using online dynamic mode decomposition, European Journal of Control 80 (2024). doi:10.1016/j.ejcon.2024.101117.

[36] C. Vega-Zambrano, N. A. Diangelakis, V. M. Charitopoulos, Data-driven model predictive control for continuous pharmaceutical manufacturing, Int J Pharm 672 (2025) 125322. doi:10.1016/j.ijpharm.2025.125322.
URL https://www.ncbi.nlm.nih.gov/pubmed/39921017

[37] J. Liu, Y. Shi, C. Ding, M. Beer, Efficient global sensitivity analysis framework and approach for structures with hybrid uncertainties, Computer Methods in Applied Mechanics and Engineering 436 (2025). doi:10.1016/j.cma.2024.117726.

[38] D. C. Liu, J. Nocedal, On the limited memory BFGS method for large scale optimization, Mathematical Programming 45 (1) (1989) 503–528. doi:10.1007/BF01589116.
URL https://doi.org/10.1007/BF01589116

[39] H. G. Weller, G. Tabor, H. Jasak, C. Fureby, A tensorial approach to computational continuum mechanics using object-oriented techniques, Computers in Physics 12 (6) (1998) 620–631. doi:10.1063/1.168744.

[40] K. Taira, T. Colonius, The immersed boundary method: A projection approach, Journal of Computational Physics 225 (2) (2007) 2118–2137. doi:10.1016/j.jcp.2007.03.005.

[41] S. Chhang, C. Sansour, M. Hjiaj, J.-M. Battini, An energy-momentum co-rotational formulation for nonlinear dynamics of planar beams, Computers & Structures 187 (2017) 50–63. doi:10.1016/j.compstruc.2017.03.021.

[42] J. Schoeftner, Shape control of moderately thick piezoelectric beams, Acta Mech 234 (8) (2023) 3091–3107. doi:10.1007/s00707-023-03539-w.
URL https://www.ncbi.nlm.nih.gov/pubmed/37457595

[43] G. Chourdakis, K. Davis, B. Rodenberg, M. Schulte, F. Simonis, B. Uekermann, G. Abrams, H. J. Bungartz, L. Cheung Yau, I. Desai, K. Eder, R. Hertrich, F. Lindner, A. Rusch, D. Sashko, D. Schneider, A. Totounferoush, D. Volland, P. Vollmer, O. Z. Koseomur, preCICE v2: A sustainable and user-friendly coupling library, Open Res Eur 2 (2022) 51. doi:10.12688/openreseurope.14445.2.
URL https://www.ncbi.nlm.nih.gov/pubmed/37645328

[44] A. Goza, T. Colonius, J. E. Sader, Global modes and nonlinear analysis of inverted-flag flapping, Journal of Fluid Mechanics 857 (2018) 312–344. doi:10.1017/jfm.2018.728.

[45] M. Lauber, G. D. Weymouth, G. Limbert, Immersed-Boundary Fluid-Structure Interaction of Membranes and Shells, Journal of Physics: Conference Series 2647 (5) (2024) 052002. doi:10.1088/1742-6596/2647/5/052002.
URL https://doi.org/10.1088/1742-6596/2647/5/052002

[46] L. Patanè, F. Sapuppo, M. G. Xibilia, Soft Sensors for Industrial Processes Using Multi-Step-Ahead Hankel Dynamic Mode Decomposition with Control, Electronics 13 (15) (2024). doi:10.3390/electronics13153047.